

Variational Sparse Paired Autoencoders (vsPAIR) for Inverse Problems and Uncertainty Quantification

Jack Michael Solomon^{†,1}, Rishi Leburu¹, and Matthias Chung¹

¹Emory University Department of Mathematics

February 11, 2026

Abstract

Inverse problems are fundamental to many scientific and engineering disciplines; they arise when one seeks to reconstruct hidden, underlying quantities from noisy measurements. Many applications demand not just point estimates but interpretable uncertainty. Providing fast inference alongside uncertainty estimates remains challenging yet desirable in numerous applications.

We propose the Variational Sparse Paired Autoencoder (vsPAIR) to address this challenge. The architecture pairs a standard VAE encoding observations with a sparse VAE encoding quantities of interest, connected through a learned latent mapping. The variational structure enables uncertainty estimation, the paired architecture encourages interpretability by anchoring QoI representations to clean data, and sparse encodings provide structure by concentrating information into identifiable factors rather than diffusing across all dimensions. To validate the effectiveness of our proposed architecture, we conduct experiments on blind inpainting and computed tomography, demonstrating that vsPAIR is a capable inverse problem solver that can provide interpretable and structured uncertainty estimates.

Keywords: Machine Learning, Inverse Problems, Uncertainty Quantification, Generative Modeling

1 Introduction

Inverse problems are central to scientific and engineering inference: from indirect and noisy measurements, one seeks to reconstruct hidden quantities that generated the data. Let \mathcal{X} denote the space of unknowns (e.g., parameters or fields) and \mathcal{Y} the space of observables, connected through a forward operator $F : \mathcal{X} \rightarrow \mathcal{Y}$. Measurements are modeled as

$$y = F(x) + \varepsilon,$$

where ε represents measurement noise or model error taking values in \mathcal{Y} . Because small perturbations in y may induce large changes in the admissible x , such problems are typically *ill-posed* in the sense of Hadamard [1].

Classical approaches address ill-posedness by introducing regularization or statistical priors. Variational methods such as Tikhonov, total variation, and sparsity-promoting penalties [2, 3] stabilize the solution through explicit constraints, while Bayesian formulations interpret both x and y as random variables and infer the posterior $p(x | y)$ via Bayes' theorem [4]. Although these approaches provide strong theoretical guarantees, they require repeated evaluation of F and careful tuning of regularization parameters, which becomes computationally demanding in high-dimensional or nonlinear settings.

More recently, there has been a shift towards *data-driven* approaches. Such approaches use parameterized neural networks to learn various attributes of the underlying inverse problem. *End-to-end* methods learn direct mappings $F^\leftarrow : \mathcal{Y} \rightarrow \mathcal{X}$ from paired samples (x, y) [5, 6]. *Prior learning* methods employ a data-driven

[†]: Corresponding author, direct questions to jack.michael.solomon@emory.edu.

prior: plug-and-play methods incorporate pretrained denoisers as implicit priors within optimization schemes [7, 8], and learned methods use regularization techniques to replace hand-crafted penalties with trainable functionals [9, 10]. Hybrid methods such as algorithm unrolling interpret iterative solvers as neural networks with learnable parameters [11, 12]. Various other methodologies exist and have been successful in a variety of applications [13].

Learning latent representations of data offers a complementary regularization strategy. Rather than prescribing a hand-crafted regularizer, one learns low-complexity latent representations directly from data and performs inversion in this learned space. *Autoencoders* and their probabilistic extensions, *variational autoencoders (VAEs)* [14], capture intrinsic manifolds of high-dimensional data and thus serve as implicit priors. Standard autoencoders impose a low-dimensional bottleneck on the deterministic latent representation which typically has the effect of reducing high frequency variations [15, 16]. Early works leveraged this regularizing property of under-complete autoencoders for applications in denoising [16, 17]. This later inspired the use of autoencoders as an end-to-end approach [18]. The implicit regularizing properties of autoencoders have also made them attractive for prior-learning where the learned distribution over the latent space captures the variability of plausible solutions and serves as a low-dimensional manifold constraint for reconstruction [19]. Recent work on *paired autoencoders* [20, 21, 13] and *latent-twin architectures* [22] extends this idea by coupling encoders and decoders in both \mathcal{X} - and \mathcal{Y} -domains, learning mappings between latent spaces that emulate both the forward and inverse operators. However, dense latent codes can entangle information, obscure uncertainty, and overfit small datasets.

A major drawback of many of the referenced approaches above is the lack of uncertainty quantification (UQ). In a Bayesian sense, UQ approximates the posterior $p(x | y)$, not merely a point estimate [4]. Many applications demand this: in medical imaging, clinicians must distinguish pathology from reconstruction artifacts; in seismic inversion, uncertainty informs drilling risk; in autonomous systems, calibrated confidence is safety-critical. Score-based diffusion methods address UQ through iterative posterior sampling [23, 24, 25]. Sample diversity reflects posterior uncertainty, but repeated network evaluations at inference sacrifice the speed of amortized approaches. The deterministic methods discussed above, including paired autoencoders, offer fast inference but lack the probabilistic structure necessary for UQ.

This motivates frameworks combining amortized inference with built-in probabilistic structure for efficient uncertainty estimation. Sparse latent representations that correspond to interpretable features would additionally clarify which data characteristics drive reconstruction, and interpretable UQ.

Contributions. We propose the Variational Sparse Paired Autoencoder (vsPAIR), a framework combining probabilistic inference, sparsity and paired latent mappings for uncertainty-aware inversion. The architecture encodes observations y via a standard VAE and sparse representations of quantities of interest x via a *sparse VAE* (sVAE), with a learned mapping connecting the two latent spaces. The sparse encoding reflects the assumption that observations are driven by few dominant factors, yielding interpretable latent codes while regularizing reconstruction. The variational structure enables posterior approximation for UQ.

The key contributions of this work are as follows:

1. The vsPAIR framework with probabilistic latent structure, enabling both fast amortized inference and interpretable uncertainty quantification.
2. Theoretical analysis of our framework in a reduced setting, justifying its use in uncertainty quantification.
3. Experimental validation on ill-posed inverse problems—blind inpainting and computed tomography (CT)—demonstrating that vsPAIR can achieve interpretable and structured uncertainty quantification alongside competitive reconstruction.

Structure of the paper. Section 2 reviews classical and learning-based formulations of inverse problems, including autoencoders and paired latent mappings. Section 3 introduces the vsPAIR framework: the paired architecture, and theoretical analysis of uncertainty quantification under simplifying assumptions. Finally,

Section 4 and Section 5 present numerical demonstrations on blind inpainting and CT, followed by concluding remarks. The introduction of sparsity in the QoI autoencoder presents technical challenges which are discussed and addressed in Section A.

Notation and Setting. Let X denote the quantity of interest (QoI) and Y the observation, interpreted as random variables with a joint distribution (X, Y) absolutely continuous with respect to Lebesgue measure, thus admitting a joint density $p(x, y)$ [26]. We use p for true distributions and q for variational approximations. Notation is summarized in Table 1.

Symbol	Description
X, Y, Z	Random variables for QoI, observation, and latent codes
x, y, z	Samples from respective distributions
$p(\cdot), q(\cdot)$	True and approximate (variational) distributions
$q_{\phi_x}(z x)$	Variational encoder for QoI with trainable parameters ϕ_x
$q_{\theta_x}(x z)$	Probabilistic decoder for QoI with trainable parameters θ_x
$q_{\phi_y}(z y)$	Variational encoder for observations with trainable parameters ϕ_y
$q_{\theta_y}(y z)$	Probabilistic decoder for observations with trainable parameters, θ_y
$\mu_{\phi_x}, \sigma_{\phi_x}, \omega_{\phi_x}$	Network outputs for that parameterize the spike-and-slab posterior
$\mu_{\phi_y}, \sigma_{\phi_y}$	Network outputs for that parameterize the Gaussian posterior
z_x, z_y	Latent samples: $z_x \sim q_{\phi_x}(z x)$, $z_y \sim q_{\phi_y}(z y)$
$M_{\theta_M}^{\leftarrow}$	Learned mapping $\mathcal{Z}_Y \rightarrow \mathcal{Z}_X$ with trainable parameters θ_M
\tilde{x}, \tilde{y}	Autoencoder reconstructions of x, y
\hat{x}, \hat{z}_x	Reconstructions of QoI and its latent representation
$\mathcal{N}(v \mu, \Sigma)$	Normal distribution with mean μ and covariance Σ
$\mathcal{SS}(v \mu, \sigma, \omega)$	Spike-and-slab distribution with parameters μ, σ and ω

Table 1: Summary of notation.

2 Background

This section reviews the classical formulations of inverse problems and the learning-based methods that motivate our approach. The reader is referred to [13] for a more in-depth exposition; we closely follow the structure and notation of this work.

Inverse problems seek to recover unknown quantities from indirect observations. We consider the forward operator $F : \mathcal{X} \rightarrow \mathcal{Y}$, which maps unknowns to observables. In many applications, this operator naturally decomposes as

$$F = P \circ u,$$

where $u : \mathcal{X} \rightarrow \mathcal{U}$ maps model parameters $x \in \mathcal{X}$ to a state $u(x) \in \mathcal{U}$ given by the solution of a governing ordinary or partial differential equation (ODE/PDE), and $P : \mathcal{U} \rightarrow \mathcal{Y}$ projects the state onto the observation space. Observations then satisfy

$$y = F(x) + \varepsilon = (P \circ u)(x) + \varepsilon,$$

with noise or model discrepancy $\varepsilon \in \mathcal{Y}$. This decomposition clarifies where computational cost concentrates, namely in solving for u , and where structural priors are specified on x and/or u .

A deterministic estimate \hat{x} is commonly obtained by minimizing a stabilized objective

$$\hat{x} = \operatorname{argmin}_{x \in \mathcal{X}} \mathcal{C}(F(x), y) + \mathcal{R}(x), \quad (1)$$

where \mathcal{C} measures data fidelity (e.g., $\|F(x) - y\|_2^2$ or a negative log-likelihood) and \mathcal{R} encodes prior structure. Canonical choices for \mathcal{R} include quadratic Tikhonov, total-variation, and ℓ^1 sparsity penalties [2, 3]. These

restore stability but require careful selection of weights and may still be expensive when F is nonlinear and high-dimensional.

The Bayesian perspective specifies a prior $p_{\text{prior}}(x)$ and likelihood $p_{\text{like}}(y | x)$, yielding the posterior

$$p_{\text{post}}(x | y) \propto p_{\text{like}}(y | x) p_{\text{prior}}(x),$$

which quantifies uncertainty in the unknown x , given observation y and prior knowledge on x , [27, 4]. Under a Gaussian noise assumption $\varepsilon \sim \mathcal{N}(\varepsilon | 0, \Gamma_y)$ and Gaussian prior $x \sim \mathcal{N}(x | m, \Gamma_x)$ with Γ_x, Γ_y symmetric positive definite, the maximum a posteriori (MAP) estimator solves

$$\min_{x \in \mathcal{X}} \frac{1}{2} \|F(x) - y\|_{\Gamma_y^{-1}}^2 + \frac{1}{2} \|x - m\|_{\Gamma_x^{-1}}^2, \quad (2)$$

which recovers the Tikhonov problem Equation (1). Thus, quadratic variational regularization corresponds to a Gaussian prior; more generally, the negative log-prior acts as a regularizer \mathcal{R} .

When one expects the unknown x to be compressible, an ℓ^1 penalty in Equation (1) corresponds to a Laplace prior, promoting sparse solutions while retaining convexity in many linear cases [28]. Such sparsity assumptions are common in imaging and geophysical inversion, and motivate the latent sparsity we later enforce in our learned surrogates [29, 30].

Both paradigms face scalability limits. Solving Equation (1) for a point-estimate via gradient-based methods typically requires repeated evaluations of F and its derivatives; sampling or approximating p_{post} may become prohibitive for nonlinear F or large $\text{dim}(\mathcal{X})$. The intractability of these solvers is further amplified for UQ. Iterative approaches such as Markov Chain Monte Carlo and Kalman Filtration require repeated computations using the forward model, which quickly render them infeasible for use in large problems without simplification or approximation [27]. Moreover, these approaches are inaccessible when F is unknown or unavailable.

These costs motivate surrogate models that reduce the expenses associated with inverse inference. Many of these methods are based around dimensionality reduction which formulate the problem in a lower dimensional space. In addition to the reducing computational costs, such approaches are attractive since the dimensionality bottleneck induces an implicit prior. Recent years have seen a surge in scientific machine learning approaches that follow this paradigm. Polynomial chaos and Gaussian processes can be effective low-dimensional surrogates [31], whereas deep neural networks can approximate complex operators in high dimension [32]. Autoencoders and VAEs [14] embrace a low-dimensional latent space as their core feature, using self-supervised learning to generate compressed representations of data. The defining feature of latent-twins approaches [22] is to learn the inversion between latent representations, which is embraced in the vsPAIR framework.

The following section (Section 2.1) provides background on autoencoders and VAEs, followed by a description of sVAEs (Section 2.2) and finally a discussion of paired autoencoders as well as the more general latent twin methodology (Section 2.3).

2.1 Autoencoders and Variational Autoencoders (VAEs)

Autoencoders have become a cornerstone of machine learning and have seen significant application in inverse problems. These models learn a parameterized mapping from the data space to itself via a latent representation. Let $\mathcal{X} \subset \mathbb{R}^n$ be the data space. An autoencoder consists of two components: a parameterized *encoder* $e_\phi : \mathcal{X} \rightarrow \mathcal{Z}$ mapping data to a latent space $\mathcal{Z} \subset \mathbb{R}^\ell$, and a parameterized *decoder* $d_\theta : \mathcal{Z} \rightarrow \mathcal{X}$ mapping back to the data space, where ϕ and θ are corresponding trainable network parameters. Together, these networks are trained such that $\tilde{x} = d_\theta \circ e_\phi(x) \approx x$. When $\ell < n$, the dimensional bottleneck encourages the model to learn compact, meaningful representations. Autoencoders are broadly classified into *undercomplete* ($\ell < n$) and *overcomplete* ($\ell > n$). Overcomplete autoencoders can also learn compressed representations of data by enforcing sparsity in the latent representation [33]. For a more extensive review on autoencoders, see [13].

Variational Autoencoders (VAEs) [14] extend traditional autoencoders into the probabilistic domain, enabling generative modeling of data. Instead of deterministic mappings, VAEs learn a parameterized

stochastic encoder or *variational posterior* $q_\phi(z | x)$ approximating the posterior over latent variables, and a parameterized probabilistic decoder or *likelihood model* $q_\theta(x | z)$ reconstructing data from latent samples. Deep Neural Networks with trainable parameters ϕ and θ are used to learn the a mapping from x to the distribution parameters of $q_\phi(z | x)$ and z to the distribution parameters of $q_\theta(x | z)$, respectively. Training maximizes the evidence lower bound (ELBO), a lower bound on the log-likelihood of the generated sample:

$$\log p(x) \geq \underbrace{\mathbb{E}_{z \sim q_\phi(z|x)} [\log q_\theta(x | z)]}_{\text{reconstruction}} - \underbrace{\text{D}_{\text{KL}}(q_\phi(z | x) || p(z))}_{\text{regularization}}, \quad (3)$$

where $p(z)$ is an assumed prior over the latent space, typically $\mathcal{N}(z | 0, I)$, and $\text{D}_{\text{KL}}(\cdot || \cdot)$ denotes the KL-divergence [34]. Under Gaussian assumptions on the probabilistic encoder and decoder as well as unit Gaussian assumption on the prior, the reconstruction term reduces to scaled mean-squared error and the KL term admits a closed form; see [35] for a comprehensive tutorial. For further simplicity, we also assume that the encoder and decoder have diagonal and unit covariances respectively. Negating Equation (3), and plugging in these expressions, we obtain the VAE objective to be minimized in training:

$$\mathcal{L}_{\text{VAE}}(\phi, \theta) = \frac{1}{2} \mathbb{E}_{z \sim q_\phi(z|x)} [\|x - \mu_\theta(z)\|^2] + \frac{1}{2} \sum_{j=1}^{\ell} (\sigma_{\phi,j}^2(x) + \mu_{\phi,j}^2(x) - 1 - \log \sigma_{\phi,j}^2(x)), \quad (4)$$

where $\mu_\phi(x)$ $\sigma_\phi(x)$ are learned neural networks to compute the mean and diagonal covariance of the encoder distribution: $q_\phi(z | x) = \mathcal{N}(z | \mu_\phi(x), \text{diag}(\sigma_\phi(x)))$; $\mu_\theta(z)$ is the learned network to compute the mean of the decoder distribution: $q_\theta(x | z) = \mathcal{N}(x | \mu_\theta(z), I)$. The $\text{diag}(\cdot)$ will be omitted for readability.

The KL regularization encourages the learned posteriors to match the prior, enabling generation by sampling $z \sim p(z)$ and decoding. However, this regularization introduces a fundamental tradeoff: pushing $q_\phi(z | x)$ toward $p(z)$ reduces the mutual information between x and z , limiting reconstruction fidelity [36]. This tension between reconstruction quality and generative structure is inherent to the VAE framework. To make stochastic sampling from the latent space compatible with gradient-based optimization, VAEs employ the *reparameterization trick*, see [14].

2.2 Variational Sparse Autoencoders (sVAE)

Variational Sparse Autoencoders (sVAEs) extend the classical VAE framework by explicitly encouraging sparse latent representations. In a typical VAE, we use a unit Gaussian prior and learn to trade off reconstruction quality against a penalty that keeps the approximate posterior close to that prior. While this Gaussian-KL penalty does encourage structured latent representations, it will utilize all of the latent dimensions regardless of whether they hold relevant information or not. In contrast, a sVAE adopts an overcomplete latent representation, often substantially larger than that of a standard VAE, and explicitly promotes sparsity by encouraging many latent coordinates to be zero.

The sVAE framework was introduced in [37], where the authors proposed using a *spike-and-slab distribution* for both the prior and variational posterior and derived the corresponding closed-form KL divergence enabling ELBO-based training. A spike-and-slab distribution consists of a *spike*, a Bernoulli random variable with probability ω of being 1, and a *slab* random variable often taking the form of a multivariate Gaussian [38]. The distribution is characterized by a mixture of the spike-and-slab and can be sampled according to the following procedure:

$$\nu \sim \text{Bernoulli}(\omega) \quad (5)$$

$$z | \nu = 0 \sim \delta_0(z) \quad \text{and} \quad z | \nu = 1 \sim \mathcal{N}(z | \mu, \sigma). \quad (6)$$

In the context of variational encoding, if we assume that each index follows a spike-and-slab distribution with a Gaussian slab, i.e.,

$$q_\phi(z_i | x) = \omega_i \mathcal{N}(z_i | \mu_i, \sigma_i) + (1 - \omega_i) \delta_0(z_i)$$

then there is a probability of ω_i of the i -th index being switched on, in which case it follows a Gaussian distribution with parameters μ_i and σ_i , and a $1 - \omega_i$ probability of being switched off and set to 0. A spike-and-slab distribution for the prior latent distribution is assumed similarly,

$$p(z_i) = \rho_i \mathcal{N}(z_i | 0, 1) + (1 - \rho_i) \delta_0(z_i), \quad (7)$$

where ρ_i denotes the prior probability of the i -th index being active. For simplicity, we assume that this probability is constant for each index, i.e., $\rho_i = \rho$. Consistent with the standard VAE, the parameters for the spike-and-slab distribution of the encoder are given by neural network outputs, dependent on x : $\mu_\phi(x), \sigma_\phi(x), \omega_\phi(x)$.

For simplicity in notation, we denote the spike-and-slab sampling process (Equation (5) and Equation (6)) as

$$z \sim \mathcal{SS}(z | \mu, \sigma, \omega). \quad (8)$$

Note $p(z_i | x)$ is not a density with respect to the Lebesgue measure since the distribution assigns non-zero probability with respect to a single point, i.e., the measure is not absolutely continuous with respect to the Lebesgue measure. This distribution should instead be interpreted as a mixture of a discrete spike and a continuous slab, where the expression above denotes the corresponding density with respect to an augmented Lebesgue measure. From the result in [37], when the slab component of both the encoder and prior are Gaussian, the KL term decomposes as

$$\text{D}_{\text{KL}}[q_\phi(z_i | x) | p(z_i)] = \omega_i \text{D}_{\text{KL}}[\mathcal{N}(z_i | \mu_i, \sigma_i^2) | \mathcal{N}(z_i | 0, 1)] + \text{D}_{\text{KL}}[\text{Bernoulli}(\omega_i) | \text{Bernoulli}(\rho)], \quad (9)$$

with the full expression over all ℓ latent dimensions given by

$$\text{D}_{\text{KL}}(q(z | x) | p(z)) = \sum_{j=1}^{\ell} \left[\frac{\omega_j}{2} (\sigma_j^2 + \mu_j^2 - 1 - \log \sigma_j^2) + (1 - \omega_j) \log \frac{1 - \omega_j}{1 - \rho} + \omega_j \log \frac{\omega_j}{\rho} \right]. \quad (10)$$

Combined with a reconstruction term for a Gaussian decoder with unit covariance, the negative ELBO for the sVAE becomes

$$\mathcal{L}_{\text{sVAE}}(\phi, \theta) = \frac{1}{2} \mathbb{E}_{z \sim q_\phi(z|x)} [\|x - \mu_\theta(z)\|^2] + \sum_{j=1}^{\ell} \left[\frac{\omega_j}{2} (\sigma_j^2 + \mu_j^2 - 1 - \log \sigma_j^2) + (1 - \omega_j) \log \frac{1 - \omega_j}{1 - \rho} + \omega_j \log \frac{\omega_j}{\rho} \right] \quad (11)$$

Training of the sVAE must be handled carefully since the immediate question of how to choose a prior sparsity level ρ arises and the Bernoulli sampling procedure further introduces complexity due to non-differentiability. These challenges are discussed in Section A, where we describe a training objective we use to learn ρ .

The benefit of sVAEs are that they typically lead to more interpretable, disentangled latent representations [37]. Because many real-world signals lie on low-dimensional manifolds, enforcing sparsity helps the model focus its capacity on the most meaningful latent factors, rather than spreading small amounts of information over all dimensions. They bridge the gap between classical sparse coding, which enforces strict zeros, and VAEs, which offer a probabilistic formulation but no mechanism for efficient sparse representation.

2.3 Paired Autoencoder Frameworks (Latent Twins)

Introduced in [22], the latent twin methodology learns mathematical operators between latent representations of quantities of interest. This approach is broadly applicable to many areas of research including PDEs, ODEs, and inverse problems and can be adjusted to encode physical constraints on the system of interest in the learned latent space. To be precise, our work builds off of paired autoencoders for inverse problems, a precursor to the latent twin architecture. Once again, we follow the notation and formulation used in [13].

Paired autoencoder frameworks for inverse problems have been studied extensively in previous works [39, 40, 21, 20]. Here, two autoencoders are learned: one for the quantity of interest $x \in \mathcal{X}$ and one for the data $y \in \mathcal{Y}$: each comprises an encoder-decoder pair $(e_{\phi_x}, d_{\theta_x})$ and $(e_{\phi_y}, d_{\theta_y})$. For ease of notation, we suppress the dependence of the encoders/decoders on trained parameters, replacing the subscript with the variable the networks are trained for; the latent spaces of these autoencoders are denoted $\mathcal{Z}_x \subset \mathbb{R}^{\ell_x}$ and $\mathcal{Z}_y \subset \mathbb{R}^{\ell_y}$, respectively. The innovation lies in jointly training mappings $M^\rightarrow : \mathcal{Z}_x \rightarrow \mathcal{Z}_y$ and $M^\leftarrow : \mathcal{Z}_y \rightarrow \mathcal{Z}_x$ to bridge these spaces, compare Figure 1. M^\rightarrow , and M^\leftarrow , are both parameterized by its respective network parameters θ_{M^\rightarrow} , and θ_{M^\leftarrow} , which are also omitted unless directly relevant to discussion. These compose surrogate forward and inversion operators that act on the latent spaces of the autoencoders.

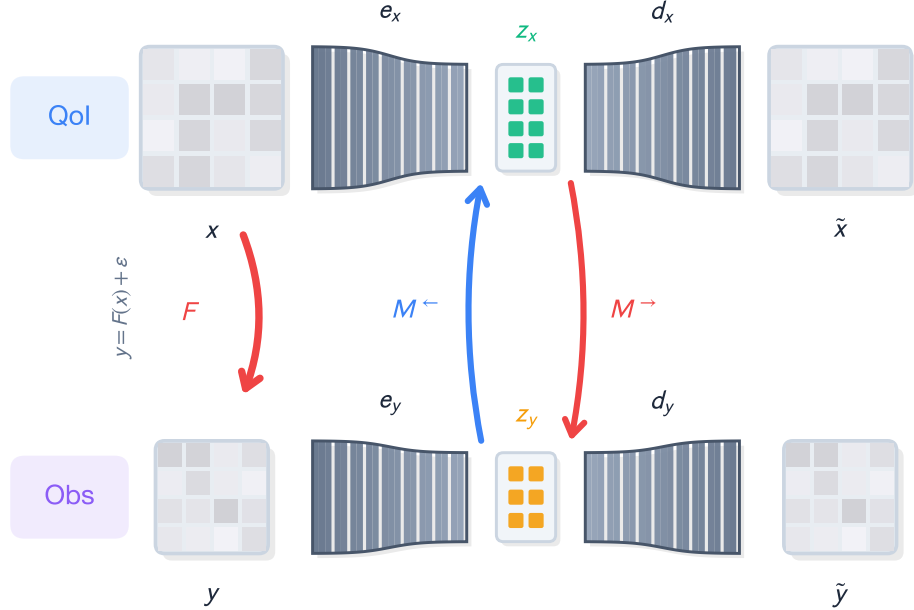


Figure 1: Deterministic paired autoencoder (PAIR) architecture where QoI and observation are related by a forward process, F : $y = F(x) + \varepsilon$. Separate Autoencoders are trained to encode the QoI (x) and observation (y), as well as surrogate forward M^\rightarrow and inversion M^\leftarrow operators that operate on the latent encoding.

Assume we are given distributions of the QoI $x \sim p(x)$ and corresponding distribution of the observation $y \sim p(y)$ connected through a forward map, F . The aim of surrogate inverse modeling is to provide a direct mapping from the observable y to the unobservable quantity x . The resulting compositions $d_y \circ M^\rightarrow \circ e_x$ and $d_x \circ M^\leftarrow \circ e_y$ provide surrogate forward

$$\hat{y} = (d_y \circ M^\rightarrow \circ e_x)(x) \quad \text{and inverse mapping} \quad \hat{x} = (d_x \circ M^\leftarrow \circ e_y)(y). \quad (12)$$

Note that the hat indicates an inferred variable using either M^\rightarrow or M^\leftarrow while the tilde indicates a direct pass through one of the autoencoders. A paired autoencoder may be learned on training data provided from the corresponding distributions by minimizing a combination of reconstruction and cross-space surrogate losses

$$\mathbb{E}_{x \sim p(x)} \mathcal{J}((d_x \circ e_x)(x), x), \quad \mathbb{E}_{y \sim p(y)} \mathcal{J}((d_y \circ e_y)(y), y), \quad (13)$$

$$\mathbb{E}_{x \sim p(x)} \mathcal{J}(d_y \circ M^\rightarrow \circ e_x(x), y), \quad \mathbb{E}_{y \sim p(y)} \mathcal{J}(d_x \circ M^\leftarrow \circ e_y(y), x). \quad (14)$$

where \mathcal{J} are appropriate losses, i.e. mean-squared-error (MSE). A design choice must be made as to whether the autoencoders are trained independently, or if the whole framework is trained together; the latter typically demonstrates better performance. For details on training paired autoencoders the interested reader

is referred to [20, 13]. In particular, our work builds off of the following innovations: [20] introduced the paired-autoencoder (PAIR) architecture that our framework is based on; [40] is a generative adaptation of the approach which instead uses Wasserstein Autoencoders [41]; [33] demonstrated the benefits of sparse overcomplete autoencoders for learning sparse embeddings of data.

These methods have been successfully applied across a wide range of problems, yet they largely produce point estimates and do not offer calibrated uncertainty quantification.

3 Methodology: vsPAIR Framework

In this section, we present the key contribution of this work: the Variational Sparse Paired Autoencoder (vsPAIR). For details on the sVAE implementation, see Section A.

3.1 vsPAIR Architecture

The vsPAIR framework pairs a standard VAE encoding observations with a sVAE encoding QoI, connected through a learned latent mapping that serves as a surrogate inversion operator. Specifically, observations are encoded via the Gaussian variational posterior $z_y \sim q_{\phi_y}(z_y \mid y)$, while the QoI is encoded using the sVAE spike-and-slab posterior $z_x \sim q_{\phi_x}(z_x \mid x)$. A trainable latent mapping $M_{\theta_M}^{\leftarrow}$ connects these two representations, mapping from the observation latent space to the QoI latent space. θ_M denotes the trainable parameters of this mapping and are suppressed for ease of notation. Inversion of an observation proceeds by encoding y to z_y , using M^{\leftarrow} to obtain a representation $\tilde{z}_x \in \mathcal{Z}_x$, and then decoding the representation to generate a reconstruction: \tilde{x} . A schematic of the architecture is shown in Figure 2.

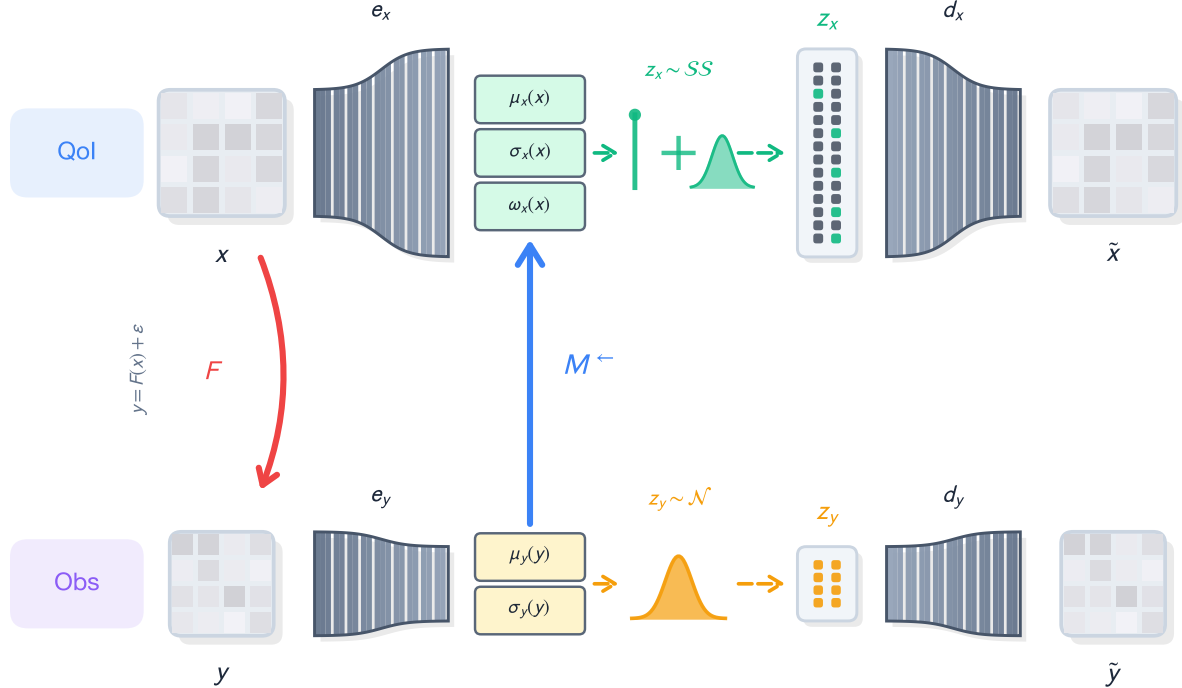


Figure 2: Schematic of the vsPAIR framework. The QoI is encoded via an sVAE producing sparse latent representations z_x , while observations are encoded via a standard VAE. The latent mapping M^{\leftarrow} operates on distribution parameters, mapping (μ_y, σ_y) to $(\hat{\mu}_x, \hat{\sigma}_x, \hat{\omega}_x)$.

Training follows the structure of the deterministic PAIR framework [21], with reconstruction losses re-

placed by the corresponding ELBOs. The complete objective is

$$\mathcal{L}(\phi_x, \theta_x, \phi_y, \theta_y, \theta_M, \rho) = \mathbb{E}_{(x,y) \sim p(x,y)} [\lambda_1 \mathcal{L}_{\text{SVAE}}(\phi_x, \theta_x) + \lambda_2 \mathcal{L}_{\text{VAE}}(\phi_y, \theta_y) + \lambda_3 \mathcal{L}_M(\theta_M) + \lambda_\rho \mathcal{L}_\rho(\rho; \alpha_0, \beta_0)], \quad (15)$$

where $\mathcal{L}_{\text{SVAE}}$ (Equation (11)) and \mathcal{L}_{VAE} (Equation (4)) are the ELBO losses for the QoI and observation autoencoders respectively, \mathcal{L}_M is the latent mapping loss defined below and $\mathcal{L}(\rho; \alpha_0, \beta_0)$ is a beta hyperprior regularization used to learn the prior sparsity level—see Section A, Equation (21). The non-negative hyperparameters $\lambda_1, \dots, \lambda_\rho$ control the relative weighting of each term.

We now address options for training the latent mapping. The first design choice that must be made is whether the autoencoders are to be trained first, and then the latent map after, or if should training proceed all together. If trained independently, then the latent codes for X do not depend on Y and a conditional independence assumption is embedded into the architecture: Z_x will be conditionally independent on Y given X ; Z_y will be conditionally independent on X given Y . Of course, this conditional independence is imposed by the model architecture and need not hold for the true underlying distribution.

On the other hand, when the encoders and latent map are trained jointly rather than independently, the model no longer enforces conditional independence between Z_x and Y (or Z_y and X), leading to a coupled latent representation that can capture richer cross-variable dependencies but at the cost of more complex theoretical analysis. The implications of this choice were extensively investigated for the deterministic case in [21], and empirically, coupled training of M^\leftarrow yielded better results.

The second design choice concerns the implementation of the latent mapping. For simplicity, we once again omit dependence on trainable parameters—that is, $\mu_{\phi_x}(x)$ is written as $\mu_x(x)$. We propose learning M^\leftarrow as a direct mapping from the distribution parameters of the observation encoder to the distribution parameters of the QoI encoder: M^\leftarrow learns to map $(\mu_y(y), \sigma_y(y))$ to $(\mu_x(x), \sigma_x(x), \omega_x(x))$ for $(x, y) \sim p(x, y)$. Here, inversion proceeds by first encoding the observation y , then computing approximate conditional distribution parameters for x , $(\hat{\mu}(y), \hat{\sigma}(y), \hat{\omega}(y))$, via M^\leftarrow , then decoding a sample \hat{z}_x from this approximate distribution to obtain \hat{x} . Generation can be accomplished by sampling the approximate latent distribution and decoding. This method provides an approximation of the posterior distribution $q(z_x | y)$ induced by the encoder conditionals, and we theoretically analyze a simplification of this approach in Section 3.2. M^\leftarrow can be trained via MSE loss between the true and approximate parameters:

$$\mathcal{L}_M(\theta_M) = \left\| \begin{bmatrix} \hat{\mu}_{\theta_M}(y) \\ \hat{\Sigma}_{\theta_M}(y) \\ \hat{\omega}_{\theta_M}(y) \end{bmatrix} - \begin{bmatrix} \mu_x(x) \\ \Sigma_x(x) \\ \omega_x(x) \end{bmatrix} \right\|_2^2 + \lambda_b \sum_{j=1}^{\ell} \hat{\omega}_j(y)(1 - \hat{\omega}_j(y)). \quad (16)$$

In order to prevent excessive averaging in the ω parameter estimation, we append an optional second term: a binary entropy penalty that encourages decisive gating predictions. This term equals zero when $\hat{\omega}_j \in \{0, 1\}$ and is maximized at $\hat{\omega}_j = 0.5$, pushing the mapping to commit to activation or deactivation rather than hedging with intermediate probabilities.

There are many other ways to train this mapping, and many techniques from generative modeling are applicable. For example, one approach is to directly match the encoded latent samples by minimizing a reconstruction loss between z_x and $M^\leftarrow(z_y)$. If an MSE loss is used here, then M^\leftarrow can approximate

$$M^\leftarrow(z_y) \approx \mathbb{E}_{z_x \sim q(z_x | x)} [Z_x | Z_y = z_y]. \quad (17)$$

In the case that $\ell_x = \ell_y$ have the same dimension, we may approach the training of M^\leftarrow as a normalizing flow between samples drawn from $q_{\phi_y}(z_y | y)$ and $q_{\phi_x}(z_x | x)$ [42]. In this case, the pushforward of $q_{\phi_y}(z_y | y)$ under M^\leftarrow is learned to approximate $q_{\phi_x}(z_x | x)$.

The vsPAIR framework, in principle, offers many advantages—in addition to sparsity representations and UQ estimation, the vsPAIR framework does not require access to the forward operator. Regarding computational cost, vsPAIR remains competitive against other methods for inference, requiring only a forward pass through the observation encoder, the latent mapping M^\leftarrow , and finally the QoI decoder to obtain a reconstruction. Moreover, after obtaining approximate distribution parameters from y , approximate posterior

samples can be generated via sampling the computed distribution and decoding. The tradeoff, however, is an expensive offline learning phase as training can be less stable and require more epochs to converge due to the sparsity constraints and the variational structure. In contrast, iterative UQ methods such as diffusion posterior sampling [23, 24, 25] have simpler training but incur repeated network evaluations at inference, as each sample requires a full iterative trajectory.

3.2 Uncertainty Quantification

At the core of the vsPAIR architecture is the interplay between sparsity and UQ. We posit that the combination of probabilistic structure and sparse encoding offers benefits beyond their individual contributions.

First, the paired architecture enables *interpretable uncertainty*. By learning separate latent representations for the QoI and observation, the QoI encoder learns features anchored to clean data rather than directly from corrupted observations. This separation of concerns means that latent dimensions encode properties of the underlying signal itself, not artifacts of the measurement process. When uncertainty arises in the latent mapping, it can be attributed to meaningful factors of the QoI. This interpretability is valuable for downstream decision-making, particularly in applications where users must understand what the model is uncertain about, not merely how much.

Second, sparse encoding yields *structured uncertainty*. In a dense VAE, uncertainty diffuses across all latent dimensions in an entangled manner. When sampling from the approximate posterior and decoding, one observes variation in reconstructions but cannot easily attribute this variation to specific factors. With sparse codes, information concentrates into a small number of active dimensions, each corresponding to a dominant factor of variation in the QoI. This concentration allows uncertainty to be traced to specific indices rather than dispersed across the full latent space.

Third, the spike-and-slab posterior naturally decomposes uncertainty into two components: *which* dimensions are active (captured by the gating probabilities ω_i) and *what values* the active dimensions take (captured by the slab parameters μ_i, σ_i). By construction, this decomposition distinguishes structural uncertainty (whether a factor is present) from parametric uncertainty (the factor’s magnitude given presence), a distinction unavailable in standard VAEs where small latent values are ambiguous between true inactivity and mere proximity to zero.

These claims are further explored and verified numerically in Section 4.

Theoretical Justification. Quantification of uncertainty often requires an estimation of the posterior distribution $p(x | y)$, and thus being able to successfully approximate this distribution is a desirable property for surrogate inversion strategies. The goal of this section is to explore the theoretical mechanism behind our framework in relation to this goal. Here, we demonstrate that sufficient training and expressiveness of the networks, generate a latent map that can approximate the latent posterior $q(z_x | y)$ induced by the paired autoencoders in a simplistic, reduced setting. Many strong assumptions are required for this result, and it is not meant to reflect a realistic setting—instead, we aim to illustrate that matches our methodology matches theory when such analysis can be performed. Note that this analysis concerns the posterior induced by the learned encoders, not the true data posterior $p(x | y)$; the gap between these is inherent to variational methods.

Spike-and-slab distributions pose analytical challenges because of the point mass at zero does not admit a Lebesgue density. For tractability, we instead reduce to the case where the variational posteriors for both x and y are Gaussian. That is, we assume that the latent representation for x , $z_x \sim q_{\phi_x}(z_x | x) = \mathcal{N}(z_x | \mu_x(x), \Sigma_x(x))$ and $z_y \sim q_{\phi_y}(z_y | y) = \mathcal{N}(z_y | \mu_y(y), \Sigma_y(y))$ where the covariances are symmetric positive definite for all x and y .

Assumptions. For the proceeding results, we make the following assumptions:

1. $\mathbb{E}[X | Y = y]$ and $\text{Cov}(X | Y = y)$ are both continuous as functions of y .
2. The variational posterior $q_{\phi_x}(z_x | x)$ is trained so that Z_x is conditionally independent of $Y | X$.

3. The mapping from x to the latent mean is affine, $\mu_x(x) = Bx + c$, and the latent covariance mapping is constant, $\Sigma_x(x) = \Sigma_{Z_x}$.

The first condition is an assumption on the true data distribution, while the second can be induced by the model architecture: this is satisfied if the two encoders are trained independently. The third depends on the networks selected for the variational posterior for the QoI and is the most restrictive assumption. Our main result is stated in Theorem 1 which establishes that the conditional mean and covariance of $Z_x | Y$ exist as a continuous function of y .

Theorem 1 *Suppose that Assumptions 1, 2, and 3 are satisfied. Then, the conditional mean and covariance of $Z_x | Y$ induced by the paired framework exist as continuous functions of y . In particular,*

$$\mathbb{E}[Z_x | Y] = B\mathbb{E}[X | Y = y] + c \quad (18)$$

and

$$\text{Cov}(Z_x | Y) = \Sigma_{Z_x} + B\text{Cov}(X | Y = y)B^\top \quad (19)$$

which is symmetric positive definite for all y .

The expressions follow directly from the tower property of conditional expectations and the law of total covariance [43], see Section C.1. The utility of Theorem 1 is that it tells us that our training objective for latent mapping is well-posed in this simplistic setup: the mapping from encoded observation parameters $(\mu_y(y), \Sigma_y(y))$ to QoI posterior parameters is continuous as a function of y , hence it can be learned by the Universal Approximation Theorem assuming sufficient network expressiveness and sufficient regularity on the expressions above [44]. This justifies training the latent mapping on paired samples of $(\mu_y(y), \Sigma_y(y))$ and $(\mu_x(x), \Sigma_x(x))$ for $(x, y) \sim p(x, y)$.

However, it does not directly imply that sampling from a Gaussian distribution with these mapped parameters match the conditional $q(z_x | y)$, since there is no guarantee that this is a Gaussian distribution. Sufficient conditions for this are given in Theorem 2.

Theorem 2 *Suppose that Y is conditionally independent of Z_x given X , and the probabilistic decoder for x , $q_{\theta_x}(x | z_x)$ is Gaussian. Furthermore, assume that data satisfy a linear, forward process $Y = AX + \varepsilon$ with ε Gaussian distributed with zero mean. Then, $q(z_x | y)$ is Gaussian distributed.*

The proof, given in Section C.2, follows from marginalization, conditional independence and results from Bayesian statistics. The utility of Theorem 2 is that under these conditions, the mapped parameters fully characterize $q(z_x | y)$: sampling an approximation $\hat{z}_x \sim \mathcal{N}(\hat{z}_x | \hat{\mu}(y), \hat{\Sigma}(y))$ with mapped parameters produces samples from the correct conditional distribution, not merely a distribution with matching moments.

Taken together, these results provide a theoretical foundation for the vsPAIR approach to uncertainty quantification under simplifying assumptions. Theorem 1 establishes that the desired latent mapping exists as an explicit function of the observations, while Theorem 2 guarantees correctness of the induced distribution in the linear-Gaussian setting. While these assumptions are restrictive, they isolate the essential mechanisms of the method and demonstrate that the proposed architecture is sound in principle. Its performance beyond this regime is investigated numerically in Section 4.

4 Numerical Results

We evaluate vsPAIR on two inverse problems: blind inpainting on MNIST and computed tomography (CT) on the LoDoPaB-CT dataset [45]. The first is a controlled setting where we examine reconstruction quality, sparsity of the learned representations, and the interpretability of uncertainty estimates. The second inverse problem concerns CT, and whether these properties hold on a larger-scale problem with more complex image structure and realistic noise. *To ensure reproducibility, elementary code will be made available on Github upon initial acceptance.* Details regarding hyperparameter tuning can be found in Section B.

4.1 Blind Inpainting on MNIST

Blind inpainting recovers an image from a corrupted observation where both the original content and the corruption mask are unknown. Unlike standard inpainting where missing regions are provided, blind inpainting must simultaneously infer what is missing and what belongs there. This is an ill-posed problem admitting multiple plausible reconstructions.

We construct a dataset from MNIST by deleting 10 randomly placed 5×5 patches from each $28 \times 28 = 784$ digit image. Patch locations are sampled independently and may overlap, with positions constrained so patches remain within the image boundary. Deleted regions are filled with the minimum pixel value. This yields 54,000 training pairs and 6,000 test pairs of corrupted observations y and clean images x .

To investigate the effects of imposing both sparsity and a probabilistic structure to our inference model, we consider four methods that systematically vary these attributes to isolate their individual contributions and demonstrate their combined effect.

- **PAIR**: Deterministic paired autoencoder with latent dimension 32 for both the observation and QoI.
- **vPAIR**: Variational paired autoencoder with Gaussian encoders, latent dimension 32 for both the observation and QoI, and a learned distributional mapping between latent spaces.
- **sVAE**: Sparse VAE mapping observations directly to QoI with no paired structure and latent dimension 784.
- **vsPAIR**: Sparse VAE with latent dimension 784 for QoI and a standard VAE with latent dimension 32 for observation.

A comparison of method properties is provided in Table 2.

Model	Sparsity	Probabilistic	Paired
PAIR	✗	✗	✓
vPAIR	✗	✓	✓
sVAE	✓	✓	✗
vsPAIR	✓	✓	✓

Table 2: Comparison of framework properties.

All models use the same convolutional neural network architecture and were trained for 100 epochs. Architecture details are provided in Section D.1. Moreover, all decoders are deterministic.

We organize the MNIST evaluation around three questions. First, how does reconstruction quality change as we introduce variational structure and sparsity? Second, do the learned latent representations capture interpretable features, and can individual dimensions be associated with semantically meaningful variation in the reconstructions? Third, does the combination of paired structure and sparsity yield structured uncertainty estimates—that is, can the model not only identify where it is uncertain but also learn latent factors that selectively control the uncertain regions? We address these questions through a combination of quantitative metrics and qualitative analyses across the four methods.

Reconstruction Quality. Table 3 reports reconstruction error and sparsity metrics across the test set. We tune the sparse models to yield a number of active dimensions comparable to the 32-dimensional dense baselines. This sparsity level is tunable via the beta distribution hyperprior parameters (α_0, β_0) , which is discussed further in Section B.

From these metrics, we observe that reconstruction quality decreases as we add variational structure and sparsity constraints: PAIR achieves the lowest MSE, followed by vPAIR, vsPAIR, and sVAE. Note that averaging over 30 posterior samples improves all variational methods, bringing their MSE close to the deterministic baseline. Additionally, the sparse methods achieve approximately 95% to 97% sparsity, with

Method	$\ell_x \ell_y$	Avg. nnz	Sparsity	MSE	MSE_{30}
PAIR	32 32	—	—	5.76×10^{-2}	—
vPAIR	32 32	—	—	6.61×10^{-2}	5.39×10^{-2}
sVAE	784	24	96.9%	8.41×10^{-2}	6.85×10^{-2}
vsPAIR	784 32	39	95.0%	7.62×10^{-2}	6.43×10^{-2}

Table 3: Reconstruction and sparsity metrics on the MNIST blind inpainting test set. $\ell_x | \ell_y$: dimensionality of the QoI latent space \mathcal{Z}_x and observation latent space \mathcal{Z}_y for paired methods, and just the latent dimension for sVAE. Avg. nnz: average number of nonzero active dimensions in \hat{z}_x obtained from the observation y for the sparse methods. Sparsity: the percentage of inactive indices. MSE: mean squared error of a single-sample reconstruction \hat{x} against the ground truth x . MSE_{30} : MSE when the reconstruction is computed as the pixel-wise mean of 30 posterior samples.

39 and 24 active dimensions for vsPAIR and sVAE on average, respectively. These results are consistent with theoretical expectations: variational structure introduces additional regularization that competes with reconstruction fidelity, consistent with standard VAE findings. We now examine whether these tradeoffs yield meaningful uncertainty estimates.

Qualitative Uncertainty Evaluation. We first analyze uncertainty quantification properties of the probabilistic architectures by sampling from the latent distributions. Drawing multiple samples from the predicted latent distribution of the QoI provides insight into where the model is uncertain. In Figure 3, we plot the reconstructions for vsPAIR, vPAIR, and sVAE, along with the corresponding variance across multiple sample draws in the latent space. This is computed for three different difficulty levels of images, as measured by the average MSE across the whole image of all three models.

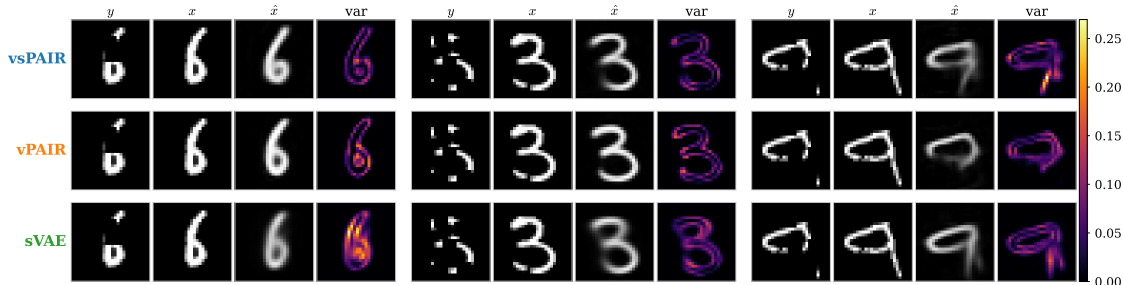


Figure 3: Reconstruction and variance comparison across variational methods. Test cases are selected at the 25th, 50th, and 96th percentile of reconstruction error averaged across all three methods, corresponding to easy, medium, and hard cases respectively. For each case, we show the corrupted observation y , ground truth x , mean reconstruction \hat{x} averaged over 30 samples from the QoI latent distribution, and the pixel-wise variance across those samples. vsPAIR is shown on the top row, vPAIR on the middle row, and sVAE on the bottom row. Higher variance in yellow indicates regions where the model produces diverse reconstructions, while lower variance in purple to black indicates confident predictions. All variance maps share a common normalized color scale.

From this visualization, a difference in how each model handles uncertainty can be observed. The first two images illustrate that in easier cases of reconstruction, all methods are most uncertain around the edges of the digits. The highest difficulty case is most revealing: the corrupted observation could reasonably be a 4, 8, or 9, and the ground truth shows a 9. vsPAIR reconstructs the digit with a noisy mean yet indicates high variance precisely in the tail region. vPAIR reconstructs primarily the known areas of the digit but produces low variance in the unknown regions. sVAE shows the highest variance overall, which is seemingly reflective

of its weaker reconstruction quality; its uncertainty estimates appear informative in the hard case but noisier across all difficulty levels. Whether the sVAE learns structured uncertainty or shows high variance because it cannot reconstruct the images is explored in the proceeding experiments.

To gain further intuition into the learned latent features, we analyze the latent representations directly. Figure 4 visualizes the latent representations for four test examples.

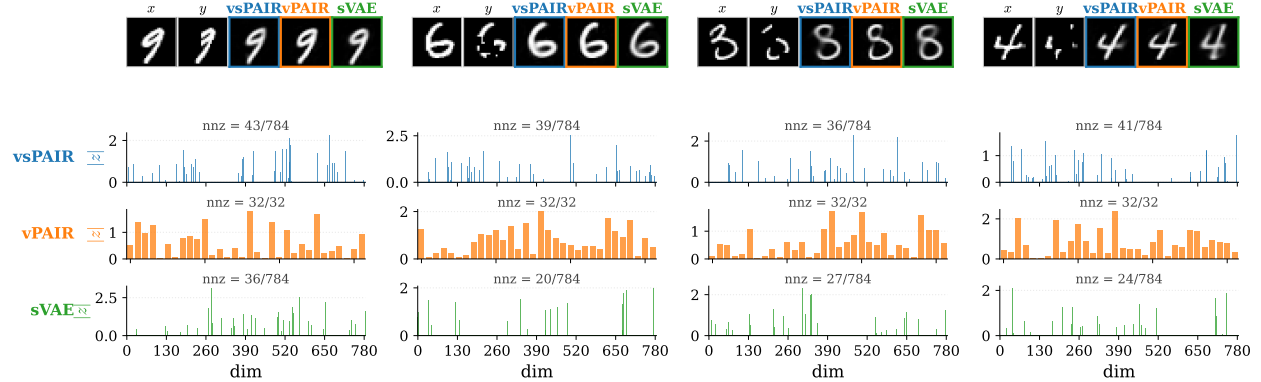


Figure 4: Sparse latent representations across methods. Top: corrupted observation y , ground truth x , and reconstructions from each method. Bottom: absolute value of each latent dimension $|z_j|$ obtained through the inversion path from y . Each bar chart is annotated with the number of nonzero dimensions.

The bar charts confirm the sparsity reported in Table 3: vsPAIR and sVAE activate only a fraction of their 784 dimensions, while vPAIR uses all 32. Using these latent encodings, we examine whether the dimensions encode interpretable features. Figure 5 takes the first example from Figure 4, the digit 9, and perturbs the three most sensitive latent dimensions for each method, where sensitivity is measured by reconstruction MSE change under perturbation.

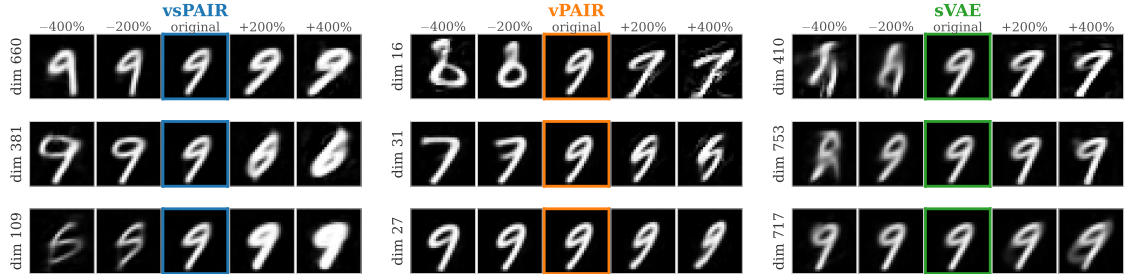


Figure 5: Latent dimension perturbation analysis for the first test example in Figure 4. For each method, we select the three latent dimensions with highest sensitivity, measured by reconstruction MSE change under perturbation. For sparse methods, we restrict to dimensions active in all 30 stochastic samples. Each image shows the mean reconstruction across 30 samples with the specified perturbation applied to that dimension. Perturbation ranges from -400% to $+400\%$ of the original value; the center column in boxes shows the unperturbed reconstruction.

The perturbation analysis suggests that all three methods learn dimensions encoding global digit structure. For instance, vsPAIR’s dimension 660 appears to control orientation, dimension 381 and 109 interpolate between digit identities, and vPAIR’s dimensions 16 and 31 similarly transition through different digits. sVAE’s dimensions seem to have less visual interpretability than the other two methods. Notably, vPAIR’s third most sensitive dimension seems to show perturbation effects that appear concentrated in the corrupted region rather than globally. This observation raises a natural question: can we systematically identify latent

dimensions that selectively control the corrupted regions of the image?

To investigate this, we search for uncertainty-localized dimensions, defined as latent dimensions whose perturbations disproportionately affect corrupted pixels relative to uncorrupted pixels. To quantify this, we define the *localization ratio*: the ratio of MSE change in corrupted regions to MSE change in uncorrupted regions under perturbation of a single latent dimension. A ratio substantially greater than 1 indicates a dimension whose effects concentrate in corrupted regions rather than affecting the reconstruction uniformly. Figure 6 displays results for vsPAIR, showing for each of three representative test images the dimension achieving the highest localization ratio.

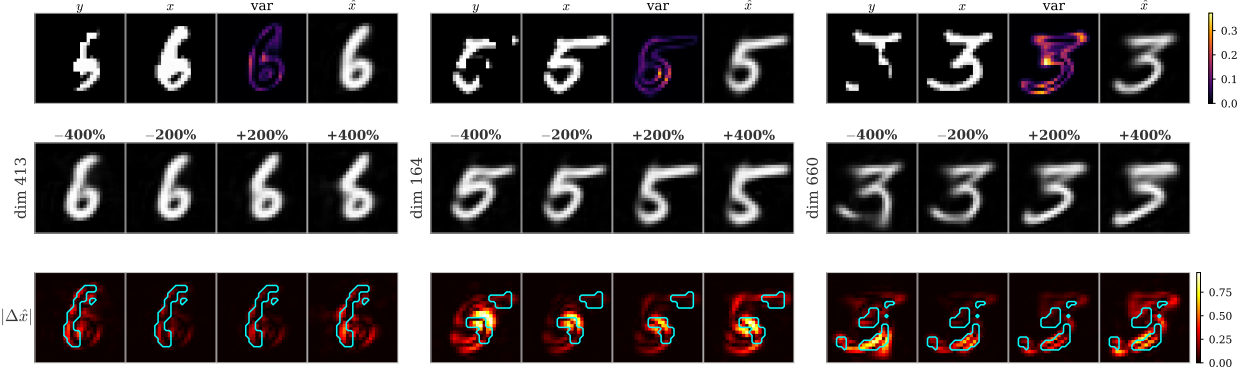


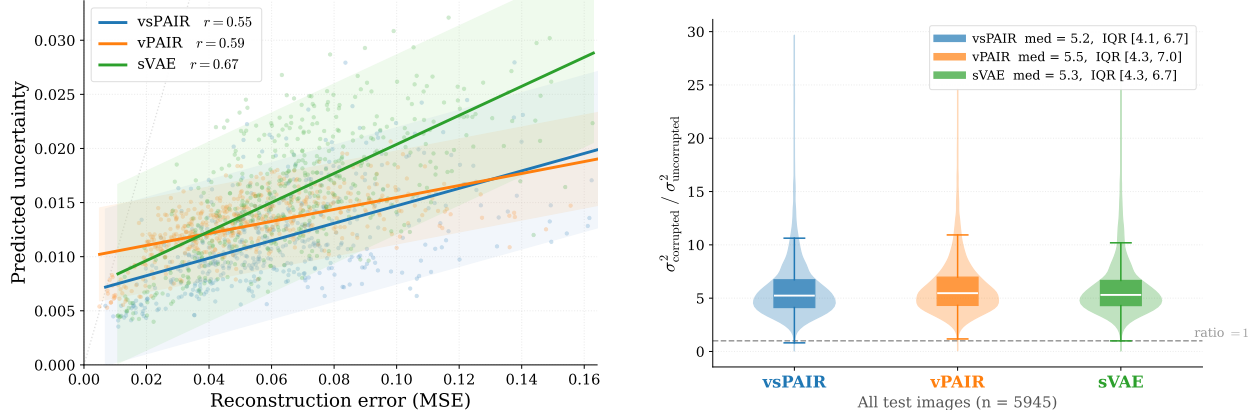
Figure 6: Uncertainty-localized latent dimensions in vsPAIR. Each column shows a representative test image selected to illustrate structured uncertainty quantification. Row 1: corrupted observation y , ground truth x , pixel-wise variance, and mean reconstruction \hat{x} . Row 2: reconstructions under perturbation of the dimension with highest localization ratio, defined as MSE change in corrupted regions divided by MSE change in uncorrupted regions, ranging from -400% to $+400\%$. Row 3: absolute reconstruction change $|\Delta\hat{x}|$ with cyan contours indicating the corruption mask.

For each test image shown, vsPAIR appears to learn at least one latent dimension whose perturbation effects concentrate within the corrupted regions, indicated by cyan contours in Row 3. The digit identity remains stable across perturbations in Row 2: a 6 remains a 6, a 5 remains a 5, while the reconstructed content in the corrupted region varies. This provides evidence that vsPAIR may be able to separate global structure from local uncertainty, with some dimensions controlling what digit is present while others control how the corrupted regions are filled in. Such a decomposition would enable interpretable uncertainty quantification, allowing identification of not just that the model is uncertain, but which latent factors drive that uncertainty and what image regions they affect.

We emphasize that these qualitative findings are inherently difficult to control or predict. There is no principled way to dictate which features an autoencoder learns, and different sparsity levels or hyperparameter choices could yield different learned representations. The specific uncertainty-localized dimensions observed here may not appear in all trained models and all test images. Nevertheless, these observations provide empirical evidence supporting the proposition that vsPAIR can learn structured and interpretable uncertainty representations.

Quantitative Uncertainty Evaluation. We provide a quantitative analysis of uncertainty quantification behavior across the variational methods and attempt to confirm the qualitative trends observed in the previous section. Figure 7 evaluates two fundamental questions: do the models know when they are wrong, and do they know where information is missing.

Figure 7a asks whether the models know when they are wrong. All three methods show moderate positive correlation between predicted uncertainty and reconstruction error, with r ranging from 0.55 to 0.67. This indicates some awareness of reconstruction difficulty. However, the scale reveals a limitation: predicted uncertainty ranges from 0.005 to 0.03, while reconstruction error ranges from 0 to 0.16. The uncertainty



Uncertainty-error correlation. Each point represents one of 500 randomly sampled test images. The x-axis shows reconstruction MSE computed as the mean of 30 samples versus ground truth. The y-axis shows predicted uncertainty as the mean pixel-wise variance across those 30 samples. Pearson correlation r is reported for each method; shaded regions indicate 95% confidence intervals for the linear fit.

Figure 7: Quantitative uncertainty evaluation on the MNIST test set.

estimates are an order of magnitude smaller than the actual errors, suggesting all models exhibit some degree of overconfidence. This is consistent with the known tendency of VAEs to produce overly narrow posteriors. sVAE shows the highest correlation at $r = 0.67$, though this may reflect its higher overall uncertainty and error rather than better calibration.

Figure 7b asks whether uncertainty concentrates in corrupted regions. All methods place approximately 5 \times more variance on corrupted pixels than uncorrupted pixels, with medians ranging from 5.2 to 5.5 and every test image having a ratio greater than 1. The models correctly identify where information is missing, not merely that information is missing.

Notably, the three methods perform similarly on both metrics. The corrupted-to-uncorrupted variance ratio appears to be a property of variational reconstruction itself rather than a distinguishing benefit of sparsity or paired structure. However, these metrics measure whether uncertainty falls on corrupted pixels, but do not capture whether uncertainty aligns with semantic ambiguity or whether the model learns latent factors that selectively control the corrupted regions.

To address this, we return to the localization ratio introduced in Figure 6, now evaluated systematically across the full test set. For each image and method, we perturb each consistently active latent dimension and identify the dimension achieving the highest localization ratio. We restrict to consistently active dimensions, defined as those active in all 30 stochastic samples, because only stable dimensions permit reliable analysis of learned factors.

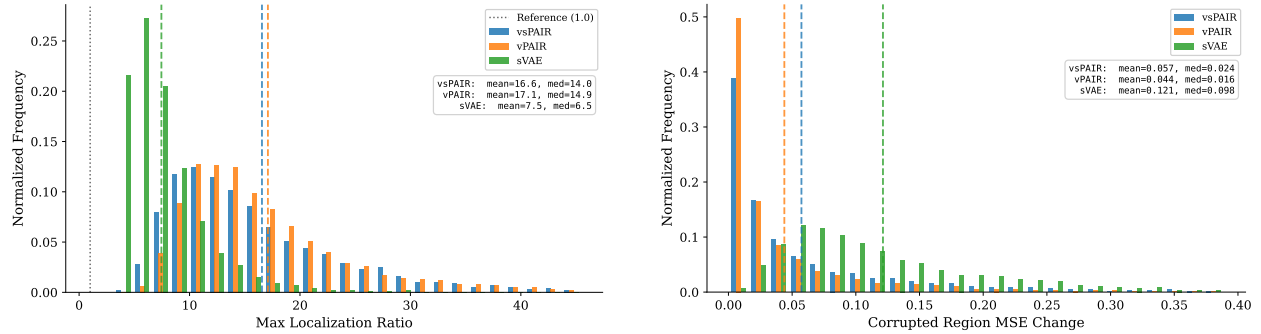
Table 4 reports the number of consistently active dimensions across methods. vPAIR uses all 32 dimensions by construction. vsPAIR maintains an average of 11.5 consistently active dimensions per image, providing a stable subset for analysis. sVAE averages only 2.6 consistently active dimensions due to its stochastic gating, limiting the pool of dimensions available for localization analysis.

The contrast between vsPAIR and sVAE is notable given that both methods employ sparse encodings. A possible explanation stems from the distributional mapping. vsPAIR predicts gating probabilities that align with the QoI encoder’s output, regularizing which dimensions activate for a given observation. sVAE learns its gates directly from corrupted observations without this anchor, potentially resulting in noisier gating decisions. This suggests that sparse encoding and paired structure together may provide both compression

	vsPAIR	vPAIR	sVAE
Always active (mean)	11.5	32.0	2.6
Always active (min)	0	32	0
Always active (max)	18	32	9

Table 4: Consistency of active latent dimensions across the MNIST test set. For each image, we count dimensions active in all 30 stochastic samples. Consistently active dimensions form the basis for the localization analysis in Figure 8, as only stable dimensions permit reliable attribution of learned factors. vPAIR uses all dimensions by construction, vsPAIR maintains a moderate stable subset, and sVAE shows high variability.

and stable factor identification, whereas sparsity alone appears insufficient.



Distribution of maximum localization ratios across the test set. For each image, we identify the consistently active dimension whose perturbation yields the highest ratio of MSE change in corrupted regions to MSE change in uncorrupted regions. Higher values indicate more selective perturbation effects concentrated in corrupted regions.

Distribution of MSE change in corrupted regions for the dimension achieving maximum localization ratio. This measures the magnitude of effect that the most localized dimension produces when perturbed, indicating how much control that dimension exerts over the corrupted region content.

Figure 8: Structured uncertainty quantification across the MNIST test set. Summary statistics are reported in Table 5.

Figure 8 shows the distribution of maximum localization ratios alongside the corresponding MSE change in corrupted regions. The histograms suggest separation between the methods, quantified in Table 5. In terms of selectivity, the paired methods achieve comparable localization ratios with medians near 14 to 15. Perturbations to their most localized dimensions affect corrupted regions roughly 14 to 15 times more than uncorrupted regions. sVAE shows lower selectivity with a median of 6.5, and a substantial fraction of images show ratios below 5. This gap persists even accounting for sVAE’s smaller pool of consistently active dimensions: when sVAE does have stable dimensions, they tend to be less selective than those of the paired methods. This provides evidence that the paired structure, which anchors the latent representation to a clean QoI encoder, may be important for learning uncertainty-localized dimensions.

It is possible that the restriction to consistently active dimensions disadvantages sVAE by excluding potentially selective but unstable dimensions. The bottom rows of Table 5 address this concern. When searching over all dimensions regardless of gating consistency, sVAE improves from median 6.5 to 8.7, but the paired methods also improve slightly to 15.1. The gap does not close, suggesting that sVAE’s limitations stem from the representations it learns rather than from the choice of which dimensions to analyze.

Figure 8 further differentiates vsPAIR from vPAIR. Despite comparable selectivity, vsPAIR produces approximately 30% larger MSE changes in corrupted regions, with mean 0.057 versus 0.044 for vPAIR. A possible interpretation is that this difference reflects how information is distributed across latent dimensions.

		vsPAIR	vPAIR	sVAE
Consistently active only	Median ratio	14.0	14.9	6.5
	Mean corrupted MSE	0.057	0.044	0.121
All dimensions	Median ratio	15.1	14.9	8.7
	Mean ratio	17.7	17.1	9.7

Table 5: Localization ratio statistics across the MNIST test set. The top rows report results when searching only over consistently active dimensions as defined in Table 4. The bottom rows report results when searching over all dimensions regardless of gating consistency. The paired methods achieve comparable selectivity in both cases, while sVAE shows lower ratios even when granted access to all dimensions.

vPAIR may spread uncertainty-relevant information across all 32 dimensions, diluting the effect of any single perturbation. vsPAIR concentrates this information into its smaller set of consistently active dimensions, approximately 11.5 on average, so each dimension carries more of the total signal.

sVAE shows the highest corrupted MSE change with mean 0.121, but this likely reflects its lack of reliable representation learning rather than concentrated information. vsPAIR’s paired architecture enables separate representation learning: the QoI encoder learns features anchored to clean images, while the distributional mapping learns to predict these features from corrupted observations. This decomposition requires additional parameters, as the paired structure naturally has greater capacity than a single encoder, but this capacity serves to separate concerns rather than simply increase expressiveness. sVAE’s single encoder must learn features directly from corrupted observations without this structural prior; sparsity provides compression but not the interpretable decomposition that may arise from the paired design.

Taken together, the qualitative and quantitative analyses provide evidence that vsPAIR can achieve a form of structured uncertainty quantification. The combination of paired structure and sparsity appears to yield latent representations where individual dimensions can both selectively target corrupted regions and produce meaningful effects when perturbed. This comes with a tradeoff: the paired architecture requires additional parameters compared to a single-encoder approach like sVAE. However, this additional capacity serves a specific architectural purpose, enabling separate representation learning for the QoI and observation spaces, which may encourage structured and interpretable latent representations. Sparsity then concentrates information into identifiable factors rather than dispersing it across all available dimensions. Whether this architectural overhead is justified depends on the application; when interpretable uncertainty quantification is a priority, the paired sparse design offers a principled path toward that goal. To illustrate that vsPAIR can be applied to more challenging inverse problems, we consider a CT inversion task.

4.2 Computed Tomography

In this section, we illustrate the vsPAIR approach on a *computed tomography* (CT) example. For this we leverage the *Low-Dose Parallel Beam CT* (LoDoPaB-CT) dataset [45], a dataset consisting of 40,000 scan slides of computed tomography images with simulated low dose measurements. This dataset uses a subset of existing high-quality CT images from the Lung Image Database Consortium and Image Database Resource Initiative [46] as ground truth images to simulate corresponding sinograms. This simulation assumes a parallel beam geometry with 1,000 projection angles, 513 projection beams, and includes Poisson-distributed noise to emulate detector noise across 4,096 detectors.

Our experimental setup treats the high-quality CT scan slices as ground truth and seeks to learn a mapping from simulated sinograms to the original scans. Consistent with the vsPAIR framework, we use a sVAE to encode the scan slide (QoI) and a standard VAE to encode the corresponding sinogram (observation). A linear mapping is then learned for the latent-space mapping.

For our experiments, we train and test on a subset of the dataset comprising 3,000 training images and 800 test images, randomly selected from the full collection. Both the original images and sinograms are cropped and down-sampled by a factor of four, yielding a QoI of size $88 \times 88 = 7,744$ and observations of

size $248 \times 128 = 31,744$. The vsPAIR model employs CNN-based encoder–decoder architectures, with latent dimensions of 8,192 for the QoI encoder and 2,048 for the observation encoder.

The first experiment establishes our method as a competitive end-to-end inversion approach. We simulate reconstruction at a variety of noise levels. The lowest level only includes simulated Poisson noise present in the LoDoPaB-CT dataset. We further generate datasets with 2.5, 5, 10 and 20% Gaussian white noise added to the sinograms in order to simulate high-noise settings. Five separate vsPAIR models were trained for 100 epochs on each noise level. Hyperparameters were configured for high-fidelity reconstructions—for details, see Section D.2.

Example results for each noise level tested are shown in Figure 9. Here, we also show reconstructions using *Filtered Back Projection* (FBP)[47] as a baseline, and compare to a more modern data-driven method, *Learned Primal-Dual* (LPD) [11, 48] which performs a standard unrolled proximal primal-dual optimization method, replacing the proximal operators with convolutional neural networks.

From Figure 9, it is evident from the results that vsPAIR offers competitive reconstruction performance to both LPD and FBP. As expected, standard iterative approaches (FBP) fail to provide meaningful reconstructions as the noise level increases, while the two data-driven approaches, LPD and vsPAIR are capable of maintaining suitable reconstructions. In particular, vsPAIR outperforms LPD for high-noise applications. It should be noted that these methods are often paired with further post-processing methods for use in practice [45], and the application of vsPAIR in these broader frameworks remains to be studied.

For the remaining results, we focus on a variable noise level, ranging from 0% to 20% Gaussian white noise in addition to the simulated Poisson noise, and aim to illustrate the UQ advantage of the vsPAIR framework. Figure 10 shows that vsPAIR provides decent reconstructions in the case of variable noise. The latent representations of the CT images had 7,041 nnz elements, on average. Moreover, implementation using variational autoencoders allows for UQ inaccessible for deterministic approaches. From Figure 10, we observe that the pixel-wise variance for each reconstruction is small, consistent with the over-confidence often exhibited by VAEs [13]. Although small, the relative value of the variances offer useful insight into the generated images. The model is often highly uncertain in regions of fine details and the edges of different regions, which are often incorrect or obscured in the reconstruction. Thus, in addition to offering competitive surrogate inversion, the vsPAIR framework is able to distinguish regions of high uncertainty through sampling of the latent variable \hat{z}_x .

Similar to the previous section, we further investigate the interpretability of the learned representations. A learned feature important for reconstruction can be distinguished by the probability that it is active. If active, the element-wise Gaussian distribution then gives insight into how confident the model is in its value. Latent features that have a high chance of activation and high variance once active therefore correspond to important yet uncertain reconstruction attributes. We confirm this by visualizing the reconstructions, as these are important yet variable features are perturbed.

Using the same approach as in the previous experiment, we analyze latent variability by perturbing the mean latent representation. We select latent features with the highest variance and activation probability exceeding 95% ($\omega_i \geq 0.95$), and visualize the resulting reconstructions as each dimension is varied by multiples of its variance. We repeat this approach for the figures with the lowest variance above the 95% threshold; see Figure 11.

The results in Figure 10 align with those of Figure 11 in that the model exhibits high uncertainty in fine details of the image. Between both images in Figure 11, we notice a consistent trend: the features with the lowest variance seemingly correspond to large dominant features of the image, while the images with the highest variance seemingly correspond to fine details. For example, in the first image (top), the perturbation of low variance features affects the outline and edges of the inner dark cavity, while perturbation of the high-variance features corresponds to the details inside the cavities, as well as the pixel values of the white structure in the center-right. This trend is evident in the second image second image (bottom), where the low-variance features indicate confidence in the structure of the image—i.e. the hole as well as the edges. Perturbation of the high-variance features also reveals a change in the pixel values surrounding the hole. From this analysis, it appears that the model is confident in the hole existing, but uncertain about the exact size or shape. It should be noted that for images uncharacteristic of the dataset, specific indices did not

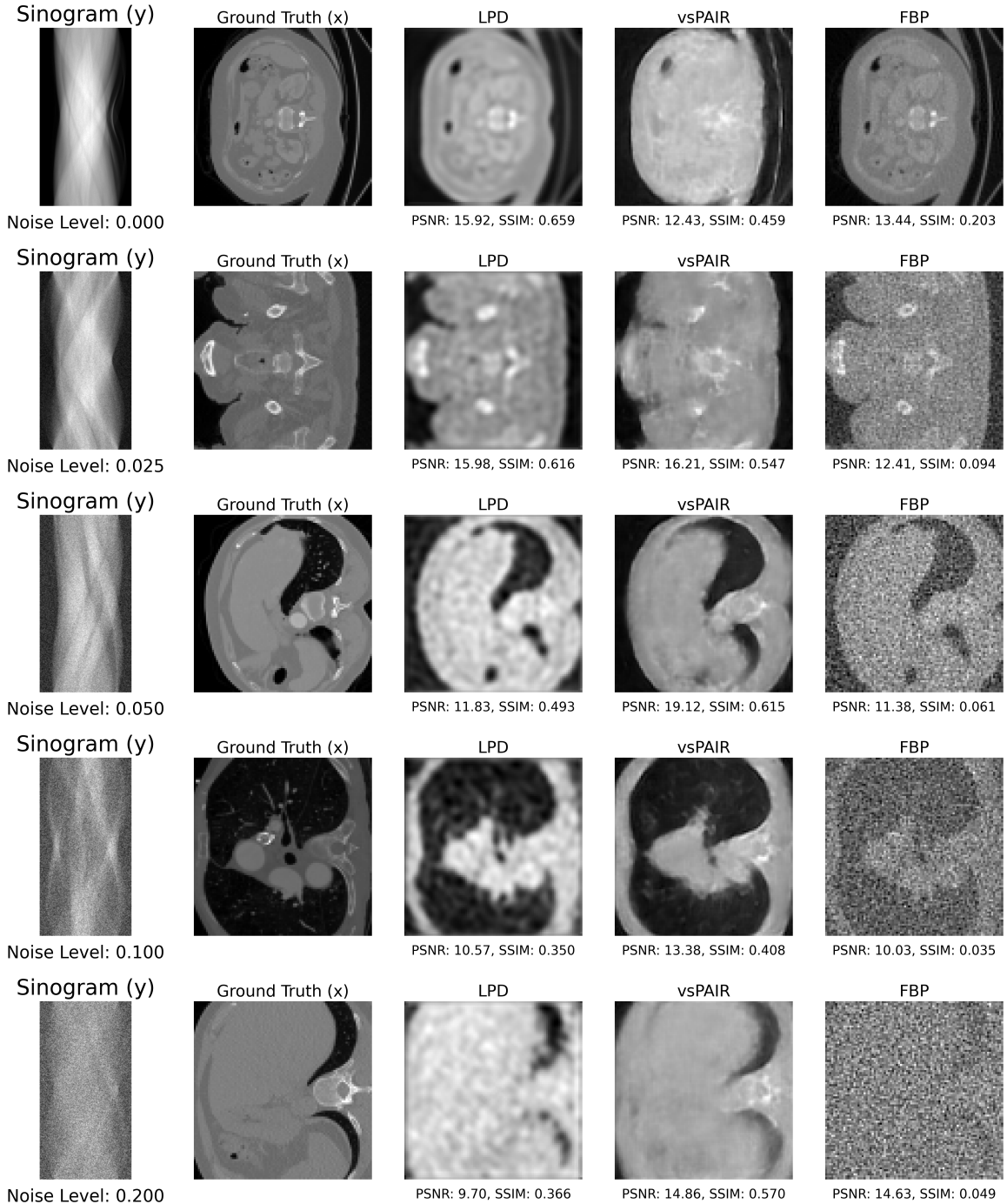


Figure 9: Example reconstruction results for different noise levels. Each row corresponds to a noise level, and columns show (left to right) the original sinogram, ground truth, LPD reconstruction, vsPAIR reconstruction, and FBP reconstruction. All images are normalized to the same [0, 1] color-scale. For the reconstructions, we report the peak signal-to-noise (PSNR) ratio as well as the structural similarity measure (SSIM) [45].

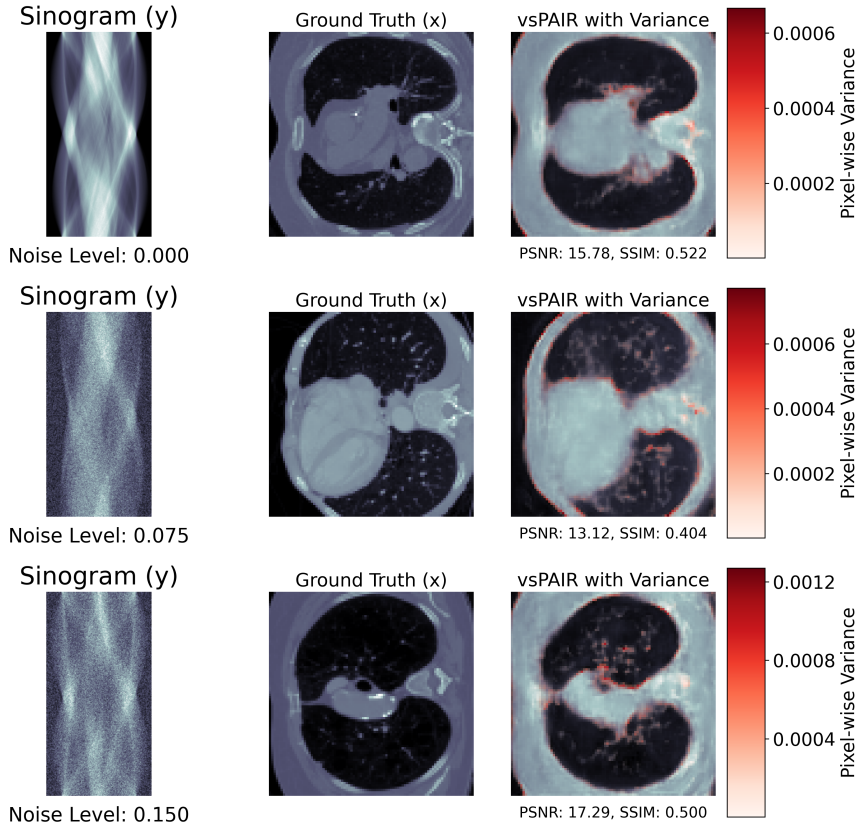


Figure 10: vsPAIR reconstructions trained in the variable noise setting. The rightmost column shows the mean overlaid with UQ estimation, generated by drawing 1,000 examples from the latent distribution, and computing the pixel-wise variance between samples. All images are normalized to the same [0, 1] color-scale.

have an interpretable effect on the reconstruction. Moreover, the latent indices that seemingly correspond to image features is heavily dependent on each specific image and the added noise.

Overall, these results suggest that the learned latent features may correspond to key aspects of the reconstructed image, and that uncertainty in these features can sometimes be understood through analysis of the predicted distribution parameters. While this interpretability is valuable for analyzing the CT images, it is less pronounced than in the MNIST experiments. Due to the higher dimensionality, more complex structure, and greater variance of these images, it is difficult to learn extremely sparse latent representations while maintaining high-fidelity reconstructions. With more active latent indices, the direct effect of each feature becomes diminished. This highlights a clear tradeoff between reconstruction fidelity and interpretability of the latent space for the vsPAIR model.

A key advantage of the vsPAIR approach over LPD and FBP is that vsPAIR does not require access to the forward operator. This certainly comes at the cost of model complexity, as the vsPAIR approaches require significantly more parameters and training time: the entire vsPAIR framework used for this example had approximately 1.1 billion parameters, while LPD only required approximately 251 thousand. Of course, various existing approaches could be leveraged to reduce the size of the vsPAIR networks [49, 50] and should be implemented for improved practicality. Additionally, a limitation of this work is that only CNN architectures are used for the models, and future work will further investigate the use of other networks and SVAE configurations.

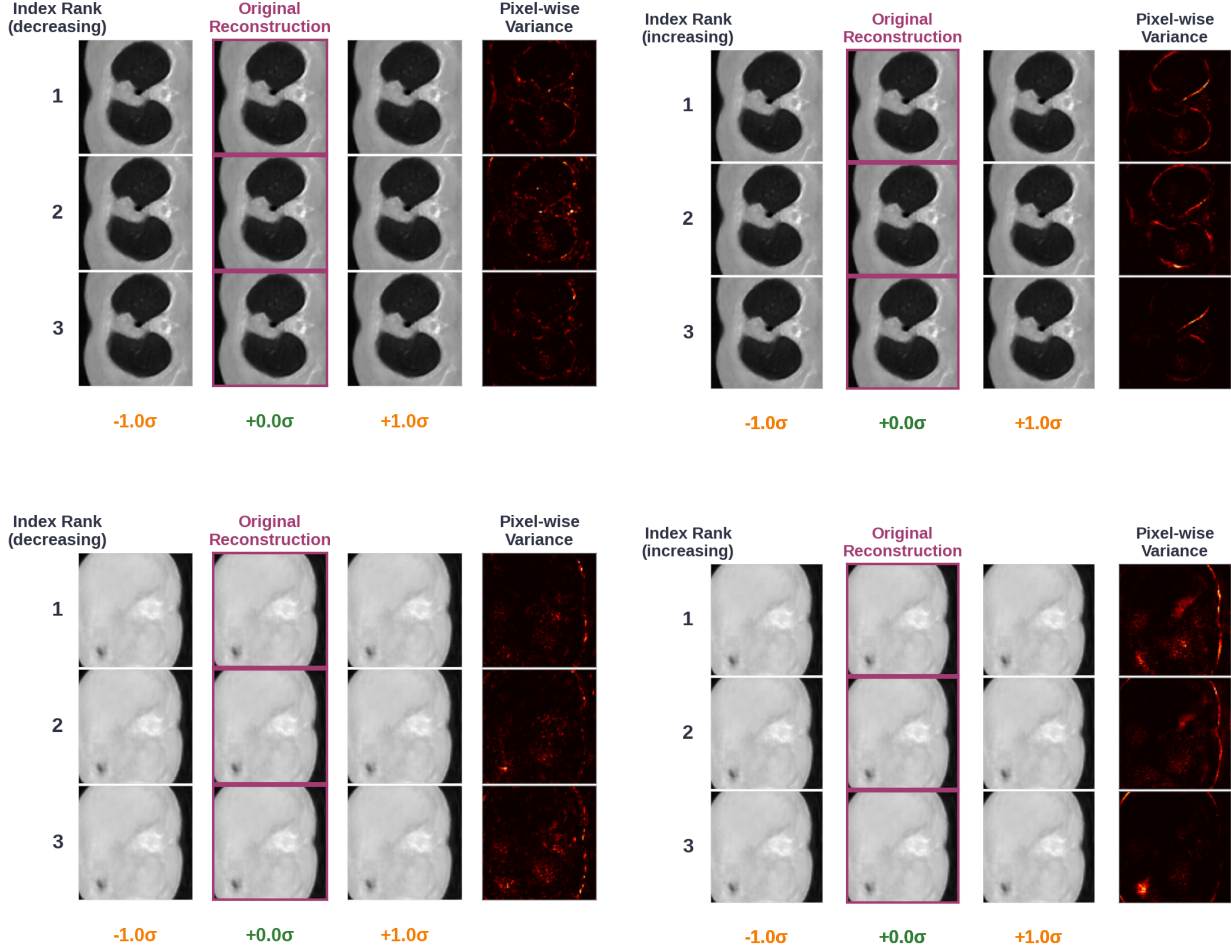


Figure 11: These figures show the effect of varying the latent indices with the top 3 highest (left) and top 3 lowest (right) variances that also have a higher than 95% chance of being active. Here, two different reconstructions are shown where the selected latent indices are varied 1 standard distributions from their mean. The rightmost column of each subplot shows the pixel-wise variance across the perturbations of the index.

5 Discussion and Conclusion

The key contribution of this work is the vsPAIR framework: a data-driven end-to-end framework suitable for fast inference with structured uncertainty. Our framework unifies generative modeling with sparse data representations, yielding low-dimensional latent structures that can support interpretable and structured uncertainty quantification. The paired architecture encourages interpretability by anchoring QoI representations to clean data, while sparsity provides structure by concentrating information into identifiable factors.

The methodology was validated both numerically and with theoretical motivation. From a theoretical standpoint, we established conditions under which the latent distribution-mapping training objective is learnable, and showed that for linear inverse problems with Gaussian noise the framework can learn a mapping to the conditional distribution of the QoI latent representation. These results rely on restrictive assumptions on the encoder and serve primarily to motivate the architecture rather than guarantee performance in general

settings: future work expands upon this analysis and further investigate the theoretical properties of paired VAE frameworks. The practical behavior of vsPAIR is assessed empirically.

Numerically, our results on the MNIST dataset demonstrated that vsPAIR offers suitable reconstructions for ill-posed inverse problems. The introduction of sparsity in the latent space resulted in sparse representations of the QoI, where active indices corresponded to key features of the reconstruction. This, coupled with the probabilistic nature of the VAE and sVAE, can enable structured UQ: an understanding of the model’s uncertainty can be generated by drawing multiple samples from the latent distribution, as well as through analysis of the distribution parameters for each likely-active index and how they affect downstream reconstruction. The CT experiments demonstrated that vsPAIR can scale to more complex inverse problems, though a thorough comparison to CT reconstruction methods and a systematic analysis of uncertainty quantification properties in this setting remain directions for future work. These capabilities come at the cost of a large model footprint and the introduction of multiple hyperparameters, though these costs are incurred during training; at inference, vsPAIR requires only forward passes through the network.

The vsPAIR approach may be considered in applications where interpretable or structured uncertainty quantification is a priority, particularly those where models can be trained offline but must be deployed efficiently (preferring cheaper inference costs). The framework will generally not match the reconstruction quality of state-of-the-art solvers, so it is best suited to problems where understanding what drives uncertainty is more valuable than maximizing fidelity. Traditional UQ methods provide aggregate measures of predictive confidence, but in many domains the critical question is not merely how much uncertainty exists but what is uncertain. In medical imaging, clinicians require uncertainty estimates that identify which features drive diagnostic ambiguity, enabling informed decisions rather than blind trust in point predictions [51, 52]. In geophysical exploration, uncertainty quantification informs drilling decisions and risk assessment; understanding whether uncertainty stems from layer boundaries versus material properties can substantially affect resource management strategies [53]. For such applications, the ability to trace uncertainty to specific latent factors, and through perturbation analysis to specific regions or features of the reconstruction, may be more valuable than well-calibrated variance estimates alone.

There are many avenues for future work. Reducing model size through compression techniques or more efficient architectures would improve scalability and more advanced implementations of sVAEs can be analyzed. Additional constraints on the latent space may further enhance semantic interpretability. The framework could also be extended to other inverse problems where interpretable uncertainty is valuable, particularly those with inherently low-dimensional structure where sparse representations may naturally align with true factors of variation.

Acknowledgments. We acknowledge Matthew T. C. Li for early discussions that inspired and clarified the scope of this work.

References

- [1] Jacques Hadamard. *Lectures on Cauchy’s problem in linear partial differential equations*. Vol. 15. Yale university press, 1923.
- [2] Curtis R Vogel. *Computational methods for inverse problems*. SIAM, 2002.
- [3] Per Christian Hansen. *Discrete Inverse Problems: Insight and Algorithms*. SIAM, 2010.
- [4] Daniela Calvetti and Erkki Somersalo. *An introduction to Bayesian scientific computing: ten lectures on subjective computing*. Vol. 2. Springer Science & Business Media, 2007.
- [5] Kyong Hwan Jin et al. “Deep convolutional neural network for inverse problems in imaging”. In: *IEEE Transactions on Image Processing* 26.9 (2017), pp. 4509–4522.
- [6] Bo Zhu et al. “Image reconstruction by domain-transform manifold learning”. In: *Nature* 555.7697 (2018), pp. 487–492.

[7] Singanallur V Venkatakrishnan, Charles A Bouman, and Brendt Wohlberg. “Plug-and-play priors for model based reconstruction”. In: *IEEE Global Conference on Signal and Information Processing*. IEEE. 2013, pp. 945–948.

[8] Yaniv Romano, Michael Elad, and Peyman Milanfar. “The little engine that could: Regularization by denoising (RED)”. In: *SIAM Journal on Imaging Sciences* 10.4 (2017), pp. 1804–1844.

[9] E Haber and L Tenorio. “Learning regularization functionals—a supervised training approach”. In: *Inverse Problems* 19.3 (Apr. 2003), p. 611. DOI: [10.1088/0266-5611/19/3/309](https://doi.org/10.1088/0266-5611/19/3/309). URL: <https://doi.org/10.1088/0266-5611/19/3/309>.

[10] Sebastian Lunz, Ozan Öktem, and Carola-Bibiane Schönlieb. *Adversarial Regularizers in Inverse Problems*. 2019. arXiv: [1805.11572 \[cs.CV\]](https://arxiv.org/abs/1805.11572). URL: <https://arxiv.org/abs/1805.11572>.

[11] Jonas Adler and Ozan Oktem. “Learned Primal-Dual Reconstruction”. In: *IEEE Transactions on Medical Imaging* 37.6 (June 2018), pp. 1322–1332. ISSN: 1558-254X. DOI: [10.1109/tmi.2018.2799231](https://doi.org/10.1109/TMI.2018.2799231). URL: [http://dx.doi.org/10.1109/TMI.2018.2799231](https://doi.org/10.1109/TMI.2018.2799231).

[12] Vishal Monga, Yuelong Li, and Yonina C Eldar. “Algorithm unrolling: Interpretable, efficient deep learning for signal and image processing”. In: *IEEE Signal Processing Magazine* 38.2 (2021), pp. 18–44.

[13] Matthias Chung, Bas Peters, and Michael Solomon. “Good Things Come in Pairs: Paired Autoencoders for Inverse Problems”. In: *arXiv preprint arXiv:2505.06549* (2025).

[14] Diederik P Kingma and Max Welling. “Auto-encoding variational bayes”. In: *arXiv preprint arXiv:1312.6114* (2013).

[15] Geoffrey E Hinton and Ruslan R Salakhutdinov. “Reducing the dimensionality of data with neural networks”. In: *Science* 313.5786 (2006), pp. 504–507.

[16] Pascal Vincent et al. “Stacked Denoising Autoencoders: Learning Useful Representations in a Deep Network with a Local Denoising Criterion”. In: *Journal of Machine Learning Research* 11.110 (2010), pp. 3371–3408. URL: <http://jmlr.org/papers/v11/vincent10a.html>.

[17] Yoshua Bengio et al. *Generalized Denoising Auto-Encoders as Generative Models*. 2013. arXiv: [1305.6663 \[cs.LG\]](https://arxiv.org/abs/1305.6663). URL: <https://arxiv.org/abs/1305.6663>.

[18] Manal Almaeен et al. “Variational Autoencoder Inverse Mapper: An End-to-End Deep Learning Framework for Inverse Problems”. In: *2021 International Joint Conference on Neural Networks (IJCNN)*. 2021, pp. 1–8. DOI: [10.1109/IJCNN52387.2021.9534012](https://doi.org/10.1109/IJCNN52387.2021.9534012).

[19] Housen Li et al. *NETT: Solving Inverse Problems with Deep Neural Networks*. 2019. arXiv: [1803.00092 \[math.NA\]](https://arxiv.org/abs/1803.00092). URL: <https://arxiv.org/abs/1803.00092>.

[20] Matthias Chung et al. “Paired autoencoders for likelihood-free estimation in inverse problems”. In: *Machine Learning: Science and Technology* 5.4 (2024), p. 045055.

[21] Emma Hart, Julianne Chung, and Matthias Chung. “A paired autoencoder framework for inverse problems via bayes risk minimization”. In: *arXiv preprint arXiv:2501.14636* (2025).

[22] Matthias Chung et al. “Latent Twins”. In: *arXiv preprint arXiv:2509.20615* (2025).

[23] Hyungjin Chung et al. “Diffusion posterior sampling for general noisy inverse problems”. In: *International Conference on Learning Representations*. 2023.

[24] Yang Song et al. “Solving inverse problems in medical imaging with score-based generative models”. In: *International Conference on Learning Representations*. 2022.

[25] Bahjat Kawar et al. “Denoising diffusion restoration models”. In: *Advances in Neural Information Processing Systems*. Vol. 35. 2022, pp. 23593–23606.

[26] Richard Durrett. *Probability: theory and examples*. Second. Belmont, CA: Duxbury Press, 1996. ISBN: 0-534-24318-5.

[27] Andrew M Stuart. “Inverse problems: a Bayesian perspective”. In: *Acta numerica* 19 (2010), pp. 451–559.

[28] Emmanuel J Candes. “The restricted isometry property and its implications for compressed sensing”. In: *Comptes rendus. Mathematique* 346.9-10 (2008), pp. 589–592.

[29] Matthias Chung and Rosemary A Renaut. “A variable projection method for large-scale inverse problems with l_1 regularization”. In: *Applied Numerical Mathematics* 192 (2023), pp. 297–318.

[30] Jack Michael Solomon, Rosemary Anne Renaut, and Matthias Chung. “Fast L_1 -regularized EEG source localization using variable projection”. In: *Inverse Problems* 41.6 (2025), p. 065014.

[31] Christopher KI Williams and Carl Edward Rasmussen. *Gaussian processes for machine learning*. Vol. 2. 3. MIT press Cambridge, MA, 2006.

[32] Kurt Hornik, Maxwell Stinchcombe, and Halbert White. “Multilayer feedforward networks are universal approximators”. In: *Neural networks* 2.5 (1989), pp. 359–366.

[33] Matthias Chung et al. “SPARSE L_1 -AUTOENCODERS FOR SCIENTIFIC DATA COMPRESSION”. In: *Journal of Machine Learning for Modeling and Computing* 6.4 (2025), pp. 51–71. ISSN: 2689-3967.

[34] Kevin P. Murphy. *Probabilistic Machine Learning: An introduction*. MIT Press, 2022. URL: <http://probml.github.io/book1>.

[35] Diederik P Kingma and Max Welling. “An Introduction to Variational Autoencoders”. In: *Foundations and Trends in Machine Learning* 12.4 (2019), pp. 307–392.

[36] Alexander A Alemi et al. “Fixing a Broken ELBO”. In: *International Conference on Machine Learning*. PMLR. 2018, pp. 159–168.

[37] Francesco Tonolini, Bjørn Sand Jensen, and Roderick Murray-Smith. “Variational Sparse Coding”. In: *Proceedings of The 35th Uncertainty in Artificial Intelligence Conference*. PMLR, Aug. 2020, pp. 690–700. (Visited on 11/11/2024).

[38] Toby J. Mitchell and John J. Beauchamp. “Bayesian Variable Selection in Linear Regression”. In: *Journal of the American Statistical Association* 83.404 (1988), pp. 1023–1032. DOI: [10.1080/01621459.1988.10478694](https://doi.org/10.1080/01621459.1988.10478694).

[39] Yoeri E. Boink and Christoph Brune. *Learned SVD: solving inverse problems via hybrid autoencoding*. 2020. arXiv: [1912.10840 \[cs.LG\]](https://arxiv.org/abs/1912.10840). URL: <https://arxiv.org/abs/1912.10840>.

[40] Moritz Piening and Matthias Chung. *Paired Wasserstein Autoencoders for Conditional Sampling*. 2024. arXiv: [2412.07586 \[cs.LG\]](https://arxiv.org/abs/2412.07586). URL: <https://arxiv.org/abs/2412.07586>.

[41] Ilya Tolstikhin et al. *Wasserstein Auto-Encoders*. 2019. arXiv: [1711.01558 \[stat.ML\]](https://arxiv.org/abs/1711.01558). URL: <https://arxiv.org/abs/1711.01558>.

[42] Jakub M. Tomczak. “Flow-Based Models”. In: *Deep Generative Modeling*. Cham: Springer International Publishing, 2024, pp. 63–92. ISBN: 978-3-031-64087-2. DOI: [10.1007/978-3-031-64087-2_4](https://doi.org/10.1007/978-3-031-64087-2_4). URL: https://doi.org/10.1007/978-3-031-64087-2_4.

[43] Joseph K. Blitzstein and Jessica Hwang. *Introduction to Probability Second Edition*. Taylor and Francis Group, 2019.

[44] Kurt Hornik, Maxwell Stinchcombe, and Halbert White. “Multilayer feedforward networks are universal approximators”. In: *Neural Networks* 2.5 (1989), pp. 359–366. ISSN: 0893-6080. DOI: [https://doi.org/10.1016/0893-6080\(89\)90020-8](https://doi.org/10.1016/0893-6080(89)90020-8). URL: <https://www.sciencedirect.com/science/article/pii/0893608089900208>.

[45] Johannes Leuschner et al. “LoDoPaB-CT, a benchmark dataset for low-dose computed tomography reconstruction”. In: *Scientific Data* 8.1 (Apr. 2021). ISSN: 2052-4463. DOI: [10.1038/s41597-021-00893-z](https://doi.org/10.1038/s41597-021-00893-z). URL: [http://dx.doi.org/10.1038/s41597-021-00893-z](https://doi.org/10.1038/s41597-021-00893-z).

[46] Samuel G. Armato III et al. “The Lung Image Database Consortium (LIDC) and Image Database Resource Initiative (IDRI): a completed reference database of lung nodules on CT scans”. In: *Medical Physics* 38.2 (Feb. 2011), pp. 915–931. ISSN: 0094-2405. DOI: [10.1118/1.3528204](https://doi.org/10.1118/1.3528204). URL: <https://www.ncbi.nlm.nih.gov/pmc/articles/PMC3041807/>.

[47] J. S. Jørgensen and W. R. B. Lionheart. “Chapter 6: Filtered Back-Projection”. In: *Computed Tomography: Algorithms, Insight, and Just Enough Theory*, pp. 73–103. DOI: [10.1137/1.9781611976670.ch6](https://doi.org/10.1137/1.9781611976670.ch6). eprint: <https://pubs.siam.org/doi/pdf/10.1137/1.9781611976670.ch6>. URL: <https://pubs.siam.org/doi/abs/10.1137/1.9781611976670.ch6>.

[48] Christian Etmann. *pytorch-primaldual*. <https://github.com/cetmann/pytorch-primaldual>. GitHub repository. 2020.

[49] Alireza Azadbakht et al. *Drastically Reducing the Number of Trainable Parameters in Deep CNNs by Inter-layer Kernel-sharing*. 2022. arXiv: [2210.14151 \[cs.CV\]](https://arxiv.org/abs/2210.14151). URL: <https://arxiv.org/abs/2210.14151>.

[50] Dongsoo Lee et al. *Learning Low-Rank Approximation for CNNs*. 2019. arXiv: [1905.10145 \[cs.LG\]](https://arxiv.org/abs/1905.10145). URL: <https://arxiv.org/abs/1905.10145>.

[51] Ling Huang et al. “A review of uncertainty quantification in medical image analysis: Probabilistic and non-probabilistic methods”. In: *Medical Image Analysis* 97 (2024), p. 103223.

[52] Moloud Abdar et al. “A review of uncertainty quantification in deep learning: Techniques, applications and challenges”. In: *Information Fusion* 76 (2021), pp. 243–297.

[53] Maria Kotsi, Alison Malcolm, and Gregory Ely. “Uncertainty quantification in time-lapse seismic imaging: a full-waveform approach”. In: *Geophysical Journal International* 222.2 (2020), pp. 1245–1263.

[54] Jakub M. Tomczak and Max Welling. *VAE with a VampPrior*. 2018. arXiv: [1705.07120 \[cs.LG\]](https://arxiv.org/abs/1705.07120). URL: <https://arxiv.org/abs/1705.07120>.

[55] Shakir Mohamed, Katherine Heller, and Zoubin Ghahramani. *Bayesian and L1 Approaches to Sparse Unsupervised Learning*. 2012. arXiv: [1106.1157 \[cs.LG\]](https://arxiv.org/abs/1106.1157). URL: <https://arxiv.org/abs/1106.1157>.

[56] Chunfeng Yuan et al. “Multi-task Sparse Learning with Beta Process Prior for Action Recognition”. In: *2013 IEEE Conference on Computer Vision and Pattern Recognition*. 2013, pp. 423–429. DOI: [10.1109/CVPR.2013.61](https://doi.org/10.1109/CVPR.2013.61).

[57] Victor Prokhorov et al. *Learning Sparse Sentence Encoding without Supervision: An Exploration of Sparsity in Variational Autoencoders*. 2021. arXiv: [2009.12421 \[cs.CL\]](https://arxiv.org/abs/2009.12421). URL: <https://arxiv.org/abs/2009.12421>.

[58] Christos Louizos, Max Welling, and Diederik P Kingma. “Learning sparse neural networks through L0 regularization”. In: *arXiv preprint arXiv:1712.01312* (2017).

[59] Yoshua Bengio, Nicholas Léonard, and Aaron Courville. *Estimating or Propagating Gradients Through Stochastic Neurons for Conditional Computation*. 2013. arXiv: [1308.3432 \[cs.LG\]](https://arxiv.org/abs/1308.3432). URL: <https://arxiv.org/abs/1308.3432>.

[60] Chris J. Maddison, Andriy Mnih, and Yee Whye Teh. *The Concrete Distribution: A Continuous Relaxation of Discrete Random Variables*. 2017. arXiv: [1611.00712 \[cs.LG\]](https://arxiv.org/abs/1611.00712). URL: <https://arxiv.org/abs/1611.00712>.

[61] Jason Tyler Rolfe. *Discrete Variational Autoencoders*. 2017. arXiv: [1609.02200 \[stat.ML\]](https://arxiv.org/abs/1609.02200). URL: <https://arxiv.org/abs/1609.02200>.

[62] Kion Fallah and Christopher J. Rozell. *Variational Sparse Coding with Learned Thresholding*. 2022. arXiv: [2205.03665 \[cs.LG\]](https://arxiv.org/abs/2205.03665). URL: <https://arxiv.org/abs/2205.03665>.

[63] Aaron van den Oord, Oriol Vinyals, and Koray Kavukcuoglu. *Neural Discrete Representation Learning*. 2018. arXiv: [1711.00937 \[cs.LG\]](https://arxiv.org/abs/1711.00937). URL: <https://arxiv.org/abs/1711.00937>.

- [64] Christopher P. Burgess et al. *Understanding disentangling in β -VAE*. 2018. arXiv: [1804.03599 \[stat.ML\]](https://arxiv.org/abs/1804.03599). URL: <https://arxiv.org/abs/1804.03599>.
- [65] Hazal Mogultay Ozcan, Sinan Kalkan, and Fatos T. Yarman-Vural. *L-VAE: Variational Auto-Encoder with Learnable Beta for Disentangled Representation*. 2025. arXiv: [2507.02619 \[cs.LG\]](https://arxiv.org/abs/2507.02619). URL: <https://arxiv.org/abs/2507.02619>.
- [66] Francesco Locatello et al. “Challenging Common Assumptions in the Unsupervised Learning of Disentangled Representations”. In: *Proceedings of the 36th International Conference on Machine Learning*. Ed. by Kamalika Chaudhuri and Ruslan Salakhutdinov. Vol. 97. Proceedings of Machine Learning Research. PMLR, June 2019, pp. 4114–4124. URL: <https://proceedings.mlr.press/v97/locatello19a.html>.
- [67] Christopher M. Bishop. *Pattern Recognition and Machine Learning (Information Science and Statistics)*. Berlin, Heidelberg: Springer-Verlag, 2006. ISBN: 0387310738.
- [68] Jean-Michel Marin and Christian P. Robert. *Bayesian Essentials with R*. Springer Texts in Statistics. New York, NY: Springer New York, 2014. ISBN: 978-1-4614-8686-2. DOI: [10.1007/978-1-4614-8687-9](https://doi.org/10.1007/978-1-4614-8687-9). URL: <http://link.springer.com/10.1007/978-1-4614-8687-9> (visited on 07/01/2021).
- [69] Diederik P. Kingma and Jimmy Ba. *Adam: A Method for Stochastic Optimization*. 2017. arXiv: [1412.6980 \[cs.LG\]](https://arxiv.org/abs/1412.6980). URL: <https://arxiv.org/abs/1412.6980>.

A sVAE Implementation Details

Beta Hyperprior for Adaptive Sparsity. Introducing sparsity into an sVAE is not trivial and a sparsity level, $(1 - \rho)$, for the prior must be specified. This can be incorporated index-wise, or fixed for all elements. [37] originally leveraged a classifier-based approach that builds off of [54], where a classifier is used to pick a specific prior for each input, based on trained pseudo-inputs. This motivates structure in the latent representations.

For simplicity, we fix the prior level of sparsity ρ for all inputs and indices, instead analyzing this problem in a Bayesian sense. We assume that the distribution of ρ is described by some underlying hyperprior distribution. We treat ρ as a learnable parameter regularized by a Beta hyperprior

$$\rho \sim \text{Beta}(\alpha_0, \beta_0). \quad (20)$$

The use of a Beta prior is common in sparse coding—see [55, 56]. In particular, our approach is similar to [57], yet different in that the previous work prescribes a Beta prior to the mixture weights of the spike-and-slab encoder, while we enforce it on the sparsity level of the prior. We consider the negative log-density as a training objective dependent on ρ ,

$$\mathcal{L}_\rho(\rho; \alpha_0, \beta_0) = (\alpha_0 - 1) \log \rho + (\beta_0 - 1) \log(1 - \rho). \quad (21)$$

Here, terms constant in ρ are dropped. The likelihood term seeks to push ρ towards a probable value under the prescribed hyperprior, but is competing with the sVAE loss term. This establishes a tradeoff between sVAE performance and sparsity, for which optimization finds a balance. Since ρ represents the prior probability of a coordinate being active, larger ρ corresponds more dense reconstructions. Setting $\alpha_0 > \beta_0$ yields a left-skewed beta density that concentrates mass toward higher values of ρ , encouraging dense latent representations. Conversely, sparsity is favored when $\alpha_0 < \beta_0$. Numerical results confirm that this approach aligns with these expectations—see Section B.

Bernoulli Relaxation. Training generative models under sparsity constraints is a well-studied field [58, 59]. A central challenge in training sVAEs arises from the non-differentiable Bernoulli sampling procedure: the loss involves quantities computed from draws of Bernoulli trials. The approach in [37], which builds off

of [60] and [61], addresses this issue via a differentiable relaxation of Bernoulli sampling based on a scaled sigmoid and we follow the notation in [37]. In particular, the latent encoding is computed element-wise as

$$z_i = T(\eta_i - 1 + \omega_i) \cdot (\mu_i + \sigma_i \epsilon) \quad (22)$$

with $\eta_i \sim \text{Uniform}(0, 1)$, and $\epsilon \sim \mathcal{N}(\epsilon | 0, 1)$. The expression involving ϵ is the standard reparameterization trick for VAEs [14], while the $T(\xi)$ is a differentiable approximation of the step function: $\mathbf{1}_{\xi \geq 0}(\xi)$, where $\mathbf{1}(\cdot)$ denotes the indicator function. This approximation is shifted to the left by $1 - \omega_i$. If this were a perfect approximation of $\mathbf{1}_{\xi \geq 0}(\xi)$, for uniform draws η_i , the outputs of $T(\eta_i - 1 + \omega_i) \sim \text{Bernoulli}(\omega_i)$. Critically, the randomness is introduced through η_i which is now decoupled from ω_i .

A Sigmoid function $\sigma(\cdot)$ can be used for T where the input is scaled by a large positive temperature parameter c . As $c \rightarrow \infty$, the scaled sigmoid converges to a step function centered at 0 with binary outputs. However, for any finite c , this relaxation cannot produce exact zeros, limiting both sparsity and interpretability.

To enforce true sparsity, we leverage a straight-through gradient estimator [59] similar to the approach used in [62]. Here, the gradient of the Bernoulli relaxation is used in backpropagation, while thresholding is used to enact exact zeros in the forward pass. This is implemented as follows:

1. Sample uniform noise $\eta_i \sim \text{Uniform}(0, 1)$.
2. Compute a relaxation of the thresholding via the differentiable step function approximation: $s_i = \sigma(c(\eta_i - 1 + \omega_i)) \in (0, 1)$, where $c > 0$ is a temperature parameter ([37, 60]).
3. Threshold to obtain exact zeros: $\hat{s}_i = \mathbf{1}_{\{s_i > 0.5\}}(s_i) \in \{0, 1\}$.
4. Straight-through gradient estimation: construct a mask, mask_i , using the thresholded values, but use the gradient of s_i for backpropagation [59, 62, 63].
5. Apply the standard reparameterization $z_i^* = \mu_i + \sigma_i \epsilon_i$ with $\epsilon_i \sim \mathcal{N}(\epsilon | 0, 1)$, then mask: $z_i = \text{mask}_i \cdot z_i^*$ [14].

B Hyperparameter Selection

The vsPAIR framework requires tuning several hyperparameters for training. Parameter estimation for scientific machine learning is an extensive area of research and largely outside the scope of this paper. However, we provide a limited analysis of how the hyperparameters affect model behavior; more robust statistical analysis and tuning methodologies remain a topic for future studies. We assume a similar set up to the one used in Section 4.1 with a few modifications—in particular, we assign equally sized latent spaces for both the QoI and observation set at 784, use $\lambda_b = 0$ to emphasize the relationship between the hyperprior and sparsity, and only train the models for 25 epochs. Empirically, we found that the performance of vsPAIR was generally robust to varied hyperparameters.

Through extensive trials varying the ratio λ_1/λ_2 , we found training remained stable and produced reasonable results up to a ratio of roughly 100. As a baseline, λ_1 and λ_2 were fixed at 1 and 0.1, respectively. This choice reflects the relative importance of x over y —we are more interested in the reconstructive and latent space properties of the QoI (x) over the observation (y) and thus we emphasize the loss of the sVAE for x in training.

We now consider the term $\lambda_\rho \mathcal{L}(\rho; \alpha_0, \beta_0)$. The effects of varying the pair (α_0, β_0) , which characterize the beta hyperprior distribution, are more interesting than the weight term λ_ρ and so we focus our analysis on the former. Recall that ρ is the probability of an index being active which is pushed towards the maximally-likely value under this hyperprior in training. For simplicity, we assume $\alpha_0, \beta_0 \geq 1$ which corresponds to a unimodal distribution. The mean is given by $\frac{\alpha_0}{\alpha_0 + \beta_0}$, and thus the higher the ratio of α_0 to β_0 , the closer the mean of this distribution is to 1. Thus, we suspect that the magnitude of the ratio $\frac{\alpha_0}{\alpha_0 + \beta_0}$ should influence the observed level of sparsity in the latent representations of \hat{z}_x . In particular, a smaller ratio corresponds to fewer active indices (sparsity); a larger ratio corresponds to a higher number of active indices (less sparsity).

Performing a coarse variation of α_0 and β_0 parameters over $[1, 2, 16, 64]$, we compute the average MSE and average nnz in \hat{z}_x and report the results in Figure 12. Here, we find that the empirical number of active indices matches the trend that we expect: higher α_0 to β_0 ratio regimes induce lower levels of sparsity, and more sparse representations can be obtained by selecting a smaller α_0 to β_0 ratio. Moreover, we observe the standard tradeoff expected in sparse representations: higher sparsity correlates to lower fidelity reconstructions.

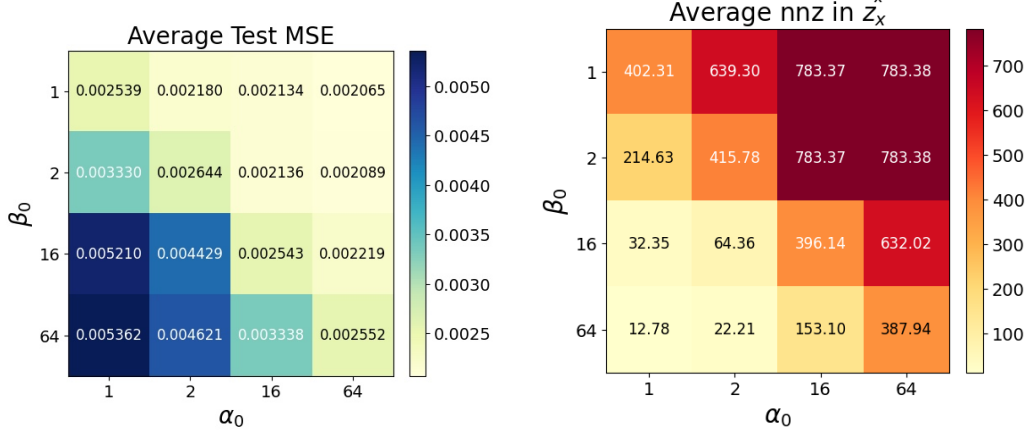


Figure 12: These heatmaps illustrate the average test set MSE (left) and average number of nnz (right) in the latent representation of \hat{z}_x , as α_0 and β_0 are varied over a coarse grid of values: $[1, 2, 16, 64]$.

Finally, we consider the coefficient of the latent-mapping loss: λ_3 . Fixing $\alpha_0 = 1$, $\beta_0 = 64$, $\lambda_1 = 1$ and $\lambda_2 = 0.1$, trials varied λ_3 across $[0.01, 0.1, 1, 10, 100]$. Resulting reconstructions exhibited insignificant variation in MSE and nnz further illustrating that the vsPAIR approach is robust to reasonable hyperparameter values.

It should be noted that the ELBOs for both the sVAE and VAE are typically broken up into a reconstruction and KL term as shown in Equation (3). It is standard to assign a hyperparameter weight to the term D_{KL} to enforce the stability of training, which is the defining characteristic of a β -VAE. The effects of this hyperparameter on VAE training are well studied in other works [64, 65, 66]. We denote the weight of the KL term in the QoI and observation ELBO as γ_x and γ_y , respectively, and found that weighting the KL terms of both sVAE and VAE by $\gamma_x = 1.0$ and $\gamma_y = 0.1$ resulted in more stable training and higher fidelity reconstructions without significantly compromising the variance of the reconstructions. Implicitly, γ_x also controls the sparsity level since it reflects the strength of the regularization that pushes the encoder to the prior. The results in the CT study used a different configuration with lower γ_x and γ_y weights to promote reconstruction accuracy.

C Theoretical Results

C.1 Proof of Theorem 1

The expression for the conditional mean follows directly from the tower property of conditional expectation and the conditional independence assumption [43]:

$$\mathbb{E}[Z_x | Y] = \mathbb{E}[\mathbb{E}[Z_x | X, Y] | Y] \quad (23)$$

$$= \mathbb{E}[\mathbb{E}[Z_x | X] | Y] \quad (24)$$

$$= \mathbb{E}[\mu_x(X) | Y] = B\mathbb{E}[X | Y] + c. \quad (25)$$

The last line follows from plugging in the affine expression for $\mu_x(X)$ and the linearity of expectation.

The covariance expression follows directly from the law of total covariance and conditional independence [43]. From this result, we have

$$\text{Cov}(Z_x | Y) = \mathbb{E}[\text{Cov}(Z_x | X, Y) | Y] + \text{Cov}(\mathbb{E}[(Z_x | X, Y)] | Y), \quad (26)$$

which by the conditional independence gives

$$\mathbb{E}(\text{Cov}(Z_x | X) | Y) + \text{Cov}(\mathbb{E}[Z_x | X] | Y). \quad (27)$$

Now, we substitute the encoder mean and covariance, which gives

$$\mathbb{E}(\Sigma_x(X) | Y) + \text{Cov}(\mu_x(X) | Y), \quad (28)$$

and simplifies to

$$\Sigma_{Z_x} + BC\text{Cov}(X | Y)B^\top \quad (29)$$

since $\Sigma_x(x)$ is constant, and $\mu_x(x)$ is affine. This is clearly symmetric positive definite as it is the sum of symmetric positive definite and symmetric positive semi-definite matrices. Continuity follows from the first assumption. More general results can be obtained by enforcing more regularity in the parameter maps and in the conditional expectation and covariance.

C.2 Proof of Theorem 2

Let $Y = AX + \varepsilon$ with ε and $p(x | z_x)$ Gaussian distributed. Writing $p(y | z_x)$ as the marginal over x , we obtain

$$p(y | z_x) = \int_X p(y, x | z_x) dx \quad (30)$$

$$p(y | z_x) = \int_X p(y | x, z_x) p(x | z_x) dx \quad (31)$$

$$p(y | z_x) = \int_X p(y | x) p(x | z_x) dx \quad (32)$$

by our conditional independence assumption. The linearity of the forward map implies that $p(y | x)$ will be Gaussian [4]. Note that this matches the marginal likelihood computation for Bayesian linear regression with a Gaussian prior. This integral can be computed in closed form, and results in a Gaussian distribution [67, 68].

By Bayes Theorem,

$$p(z_x | y) \propto p(y | z_x) p(z_x) \quad (33)$$

which is Gaussian, under the prior assumption that $p(z_x)$ is Gaussian as it constitutes the product of two Gaussian densities. The result in Theorem 2 is obtained by replacing $p(x | z_x)$ by $q_{\theta_x}(x | z_x)$.

D Model Architectures and Training Details

D.1 MNIST Example

This section details the network architectures and hyperparameter choices used for the MNIST examples.

D.1.1 MNIST Model Details

All models for the MNIST blind inpainting experiment share a common convolutional (CNN) encoder–decoder backbone and differ only in the encoder type, latent dimensionality, and inter-space mapping. Input images are single-channel 28×28 with greyscale values normalized between 0 and 1.

Each encoder block consists of the following sequence:

$$\text{Conv2D} \rightarrow \text{BatchNorm2D} \rightarrow \text{SiLU} \rightarrow \text{Conv2D} \rightarrow \text{BatchNorm2D} \rightarrow \text{AvgPool2D}(2). \quad (34)$$

The full encoder network is detailed in Table 6.

Layer	Operation	Channels	Output shape
0	Input	—	$1 \times 28 \times 28$
1	Conv2D (3×3)	$1 \rightarrow 16$	$16 \times 28 \times 28$
2	Equation (34)	$16 \rightarrow 32$	$32 \times 14 \times 14$
3	Equation (34)	$32 \rightarrow 64$	$64 \times 7 \times 7$
4	Flatten	—	3,136
5	Linear (μ)	$3,136 \rightarrow \ell$	ℓ
6	Linear ($\log \sigma^2$)	$3,136 \rightarrow \ell$	ℓ
7	Linear ($\log \omega$)	$3,136 \rightarrow \ell$	ℓ

Table 6: CNN network used for the sVAE encoder in the MNIST example. The last 3 layers correspond to each of the sVAE parameters: μ , $\log \sigma^2$, and $\log \omega$. For deterministic encoders, only a single linear head is used; for variational encoders, two heads (μ , $\log \sigma^2$) are used.

The decoders are deterministic and were implemented using a symmetric architecture, where each decoder block replaces the pooling with upsampling:

$$\text{Upsample}(2 \times) \rightarrow \text{Conv2D} \rightarrow \text{BatchNorm2D} \rightarrow \text{SiLU} \rightarrow \text{Conv2D}. \quad (35)$$

Further details are outlined in Table 7. All convolutions use kernel size 3×3 , stride 1, and padding 1.

Layer	Operation	Channels	Output shape
0	Input (Latent Vector)	—	ℓ
1	Linear	$\ell \rightarrow 3,136$	3,136
2	Reshape	—	$64 \times 7 \times 7$
3	Equation (35)	$64 \rightarrow 32$	$32 \times 14 \times 14$
4	Equation (35)	$32 \rightarrow 16$	$16 \times 28 \times 28$
5	Conv2D (3×3)	$16 \rightarrow 1$	$1 \times 28 \times 28$

Table 7: CNN network used for the sVAE decoder in the MNIST example.

Encoder Variants. Three encoder types are used across the model variants:

- *Deterministic encoder.* The flattened features are projected to a latent code $z \in \mathbb{R}^\ell$ by a single linear layer.
- *Variational encoder.* Two linear heads produce $\mu, \log \sigma^2 \in \mathbb{R}^\ell$; samples are drawn via the reparameterization trick $z = \mu + \sigma \odot \epsilon$, $\epsilon \sim \mathcal{N}(\epsilon \mid 0, I)$.
- *Sparse variational encoder.* Three linear heads produce $\mu, \log \sigma^2, \log \omega \in \mathbb{R}^\ell$. Probabilities $\omega_i \in (0, 1]$ are obtained via a clamped exponential $\omega = \exp(-\text{ReLU}(-\log \omega))$. Samples are drawn using the Bernoulli relaxation with temperature $c = 50$ and straight-through estimation (see Section A).

Model Configurations. Table 8 summarizes the architecture of each model variant. All models were trained for 100 epochs with the Adam optimizer [69] at learning rate 10^{-4} and batch size 64.

Model	x -encoder	y -encoder	ℓ_x	ℓ_y	Parameters
PAIR	Deterministic	Deterministic	32	32	687,042
vPAIR	Variational	Variational	32	32	899,490
sVAE	Sparse Var.	—	784	—	9,979,106
vsPAIR	Sparse Var.	Variational	784	32	13,067,043

Table 8: MNIST model architectures and parameter counts. ℓ_x and ℓ_y denote the QoI and observation latent dimensions, respectively.

PAIR uses two deterministic encoders and decoders with a linear latent mapping $M^\leftarrow : \mathbb{R}^{32} \rightarrow \mathbb{R}^{32}$ (1,056 parameters). vPAIR replaces both encoders with variational encoders and uses a 3-layer MLP with LayerNorm and ReLU activations as the parameter mapper $M^\leftarrow : \mathbb{R}^{64} \rightarrow \mathbb{R}^{64}$ (mapping $(\mu_y, \log \sigma_y^2) \mapsto (\hat{\mu}_x, \widehat{\log \sigma_x^2})$; 12,736 parameters; hidden dimension 64). sVAE is a standalone sparse variational autoencoder that encodes the observation y directly and decodes to x , with no paired structure or latent mapping. vsPAIR uses a sparse variational encoder for x ($\ell_x = 784$), a standard variational encoder for y ($\ell_y = 32$), and a 3-layer MLP parameter mapper $M^\leftarrow : \mathbb{R}^{1,568} \rightarrow \mathbb{R}^{2,352}$ (mapping $(\mu_y, \log \sigma_y^2) \mapsto (\hat{\mu}_x, \widehat{\log \sigma_x^2}, \hat{\omega}_x)$; 2,644,560 parameters; hidden dimension 816).

D.1.2 MNIST Hyperparameters and Training Details

Table 9 lists the training hyperparameters for each model. For the sparse models (sVAE and vsPAIR), the

Hyperparameter	PAIR	vPAIR	sVAE	vsPAIR
λ_1	1.0	1.0	1.0	1.0
λ_2	0.5	0.5	—	0.5
λ_3	1.0	1.0	—	1.0
λ_ρ	—	—	1.4	1.4
α_0	—	—	1.0	1.0
β_0	—	—	127.0	127.0
γ_x	—	1.0	1.0	1.0
γ_y	—	0.1	—	0.1
λ_b	—	—	—	0.05
Training Parameter				
nEpochs	100	100	100	100
Learning Rate	1e-4	1e-4	1e-4	1e-4

Table 9: Training hyperparameters for the MNIST experiment. λ_1 , λ_2 , and λ_3 denote the weights for the SVAE ELBO, VAE ELBO, and latent mapping loss, respectively. For PAIR, ELBOs are replaced with MSE. γ_x and γ_y , weight the KL divergence terms within each ELBO. λ_ρ weights the beta hyperprior loss. α_0, β_0 parameterize the beta hyperprior $\text{Beta}(\alpha_0, \beta_0)$ for the learned sparsity level ρ . λ_b is the binary entropy penalty weight on predicted gate probabilities.

beta hyperprior is set to $\text{Beta}(1, 127)$, which has mean $\frac{1}{128} \approx 0.008$ and concentrates near zero, encouraging high sparsity (i.e., a high prior probability ρ of each dimension being inactive). The Bernoulli approximation temperature is $c = 50$ for all sparse models. PAIR uses only MSE reconstruction losses (no KL terms), with the QoI and observation reconstruction weighted by λ_1 , respectively λ_2 .

D.2 CT Example

This section details the network architectures and hyperparameter choices used for the CT examples.

D.2.1 CT Model Details

CNN architectures were used for the encoder and decoder for the CT case study. Each encoder block consists of the following sequence:

$$\text{Conv2D} \rightarrow \text{BatchNorm2D} \rightarrow \text{SiLU} \rightarrow \text{Conv2D} \rightarrow \text{BatchNorm2D} \rightarrow \text{AvgPool2D}(2). \quad (36)$$

The full network is detailed in Table 10. All convolutions use kernel size 3×3 , stride 1, and padding 1.

Layer	Operation	Channels	Output shape
0	Input	—	$1 \times 88 \times 88$
1	Conv2D (3×3)	$1 \rightarrow 16$	$16 \times 88 \times 88$
2	Equation (36)	$16 \rightarrow 32$	$32 \times 44 \times 44$
3	Equation (36)	$32 \rightarrow 64$	$64 \times 22 \times 22$
4	Equation (36)	$64 \rightarrow 128$	$128 \times 11 \times 11$
5	Flatten	—	15,488
6	Linear	$15,488 \rightarrow 8,192$	8,192
7	Linear	$15,488 \rightarrow 8,192$	8,192
8	Linear	$15,488 \rightarrow 8,192$	8,192

Table 10: CNN network used for sVAE encoder in CT example. The last 3 layers correspond to each of the sVAE parameters: μ , $\log \sigma^2$ and $\log \omega$.

The VAE encoder for the observation data featured an identical structure, yet fitted to the dimensions of the sinogram (248×148) and a latent-space of dimension 2,048. The latent mapping was implemented as a simple linear mapping from dimensions $2 \times 2,048 \rightarrow 3 \times 8,192$.

Both decoders are deterministic and were implemented using a symmetric architecture, where each decoder block replaces the pooling with up-sampling:

$$\text{Upsample}(2 \times) \rightarrow \text{Conv2D} \rightarrow \text{BatchNorm2D} \rightarrow \text{SiLU} \rightarrow \text{Conv2D}. \quad (37)$$

Further details are outlined in Table 11. All Convolutions use kernel size 3×3 with stride 1, and padding 1. The LPD models used adapt the implementation and networks in [48] for our down-sampled setting; LPD

Layer	Operation	Channels	Output shape
0	Input (Latent Vector)	—	8,192
1	Linear	—	15,488
2	Reshape	—	$128 \times 11 \times 11$
3	Equation (37)	$128 \rightarrow 64$	$64 \times 22 \times 22$
4	Equation (37)	$64 \rightarrow 32$	$32 \times 44 \times 44$
5	Decoder block 3 Equation (37)	$32 \rightarrow 16$	$16 \times 88 \times 88$
6	Conv2D (3×3)	$16 \rightarrow 1$	$1 \times 88 \times 88$

Table 11: CNN Network used for the sVAE decoder in the CT example.

models were trained for 500 epochs with learning rate 1e-4 and batchsize 2.

D.2.2 CT Hyperparameters and Training Details

Two different sets of parameters were used to train the models showcased Figure 9 and those in Figure 10 and Figure 11. The primary difference is that sparsity was enforced strongly in the latter, while the former

targeted high-fidelity reconstructions. Correspondingly, the respective pairs (α_0, β_0) differ between the two. All hyper- and training parameters are listed in Table 12. The KL weights are notably lower than the MNIST experiment, since we focus on the fidelity of the reconstruction. We use a batch size of 2 for all training.

Hyperparameter	Figure 9 Value	Figure 10 & Figure 11 Value
λ_1	1.0	1.0
λ_2	0.1	0.1
λ_3	1.0	1.0
λ_ρ	1.0	1.0
α_0	502.0	1.0
β_0	1.0	64.0
γ_x	1e-4	1e-4
γ_y	1e-4	1e-4
λ_b	0	0
Training Parameter		
nEpochs	100	200
Learning Rate	1e-5	1e-5

Table 12: Enumeration of the hyperparameters relevant to training, and the corresponding value. Descriptions of hyperparameters can be found in Table 9.

All networks were optimized using the Adam optimizer [69].